

Superelevation and overspill control secondary flow dynamics in submarine channels

R. M. Dorrell,¹ S. E. Darby,¹ J. Peakall,² E. J. Sumner,^{2,3} D. R. Parsons,⁴ and R. B. Wynn³

Received 7 March 2013; revised 10 June 2013; accepted 17 June 2013; published 13 August 2013.

[1] In subaerial and submarine meander bends, fluid flow travels downstream in a helical spiral, the structure of which is determined by centrifugal, hydrostatic, baroclinic, and Coriolis forces that together balance frictional stresses generated by the flow. The sense of rotation of this helical flow, and in particular, whether the near bed flow is directed toward the inner bank, e.g., “river-normal,” or outer bank, e.g., “river-reversed,” is crucial to the morphodynamic evolution of the channel. However, in recent years, there has been a debate over the river-normal or river-reversed nature of submarine flows. Herein, we develop a novel three-dimensional closure of secondary flow dynamics, incorporating downstream convective material transport, to cast new light on this debate. Specifically, we show that the presence of net radial material transport, arising from flow superelevation and overspill, exerts a key control on the near bed orientation of secondary flow in submarine meanders. Our analysis implies that river-reversed flows are likely to be much more prevalent throughout submarine-canyon fan systems than prior studies have indicated.

Citation: Dorrell, R. M., S. E. Darby, J. Peakall, E. J. Sumner, D. R. Parsons, and R. B. Wynn (2013), Superelevation and overspill control secondary flow dynamics in submarine channels, *J. Geophys. Res. Oceans*, 118, 3895–3915, doi:10.1002/jgrc.20277.

1. Introduction

[2] Submarine channels can extend for thousands of kilometers and are some of the most significant geomorphological systems on the planet [Chough and Hesse, 1980]. The turbidity currents that flow through these channels are the main mechanism by which clastic sediment is transported from the continental shelf to the deep ocean [Amos *et al.*, 2010; Meiburg and Kneller, 2010], where it is deposited on submarine fans, forming some of the largest sedimentary bodies on Earth [Curray *et al.*, 2002]. However, our understanding of submarine fan dynamics and evolution remains underdeveloped [Peakall *et al.*, 2000; Kolla *et al.*, 2007; Wynn *et al.*, 2007; Kane *et al.*, 2008], in part due to the difficulties involved in observing and measuring natural subaqueous density currents. Consequently, most of our understanding of submarine gravity currents is based on (1) limited field measurements taken within sub-

marine canyon-channel environments [Paull *et al.*, 2002; Khripounoff *et al.*, 2003; Xu *et al.*, 2004; Best *et al.*, 2005; Vangriesheim *et al.*, 2009; Xu, 2010; Parsons *et al.*, 2010; Xu *et al.*, 2013]; (2) laboratory measurements [Imran *et al.*, 2002; Keevil *et al.*, 2006; Corney *et al.*, 2006; Straub *et al.*, 2008; Islam and Imran, 2008; Sequeiros *et al.*, 2010; Cossu and Wells, 2010; Straub *et al.*, 2011; Abad *et al.*, 2011; Janocko *et al.*, 2013; Ezz *et al.*, 2013]; or (3) inferences made from numerical simulations [Mulder *et al.*, 1997; Imran *et al.*, 1999; Pirmez and Imran, 2003; Das *et al.*, 2004; Meiburg and Kneller, 2010; Lesshafft *et al.*, 2011; Giorgio Serchi *et al.*, 2011; Mahdinia *et al.*, 2012; Janocko *et al.*, 2013]. However, the applicability of these diverse studies to generalized submarine channel environments remains unclear.

[3] The secondary flow circulation, and in particular, the direction of the near-bed transverse flow, imparts a strong influence on bed morphology and patterns of surface grain-sorting in meander bends. Such effects have been documented in classical studies of fluvial meanders [Engelund, 1974; Parker and Andrews, 1985; Bridge, 1993] and, more recently, in physical and numerical modeling [Peakall *et al.*, 2007; Darby and Peakall, 2012] and outcrop studies [Pyles *et al.*, 2012] of submarine channels. The secondary flow circulation in submarine meander bends may exhibit the same sense as subaerial river channels, where the near bed transverse flow is oriented toward the inner bank (“river-normal” flows [e.g., Rozovskii, 1957; Imran *et al.*, 2007, 2008; Islam and Imran, 2008]). However, theoretical, experimental, and field studies have also shown that secondary flow within submarine meander bends may also exhibit a reversed sense of circulation (“river-reversed” flows [e.g., Corney *et al.*, 2006, 2008; Keevil *et al.*, 2006,

Additional supporting information may be found in the online version of this article.

¹Geography and Environment, University of Southampton, Southampton, UK.

²School of Earth and Environment, University of Leeds, Leeds, UK.

³Ocean and Earth Science, National Oceanography Centre Southampton, University of Southampton, Southampton, UK.

⁴School of Geography, Earth and Environment Sciences, University of Hull, Hull, UK.

Corresponding author: R. M. Dorrell, Geography and Environment, University of Southampton, Southampton SO17 1BJ, UK. (r.m.dorrell@soton.ac.uk)

©2013. American Geophysical Union. All Rights Reserved. 2169-9275/13/10.1002/jgrc.20277

2007; Amos *et al.*, 2010; Parsons *et al.*, 2010; Abad *et al.*, 2011; Pyles *et al.*, 2012; Huang *et al.*, 2012), in which the near-bed transverse flow is oriented toward the outer bank.

[4] The sense of secondary flow circulation in submarine density currents is controlled by the balance of the forces acting against the shear stress generated by the flow. Within the classical Rozovskiiian framework [Rozovskii, 1957], these forces comprise centrifugal and radial pressure gradients. Extending these concepts to submarine flows, subsequent work [Corney *et al.*, 2008; Abad *et al.*, 2011] shows that both river-normal and river-reversed secondary flow are possible. The analysis of Abad *et al.* [2011] represents a significant contribution to our understanding of secondary flows in contemporary and relic submarine channel systems as it allows a quantification of the force balance and hence secondary flow regime within submarine meanders as a function of environmental parameters (specifically the densimetric Froude number and bed roughness) that may either be estimated directly or which can be reconstructed using morphological data that are readily available from hydrographic surveys (see Figure 1). Further, the study of Abad *et al.* [2011] suggests that river-reversed flow regimes are likely to be prevalent in supercritical flows, when centrifugal forces dominate transverse pressure gradient forces near the base of the flow, in the proximal regions of submarine canyon-fan systems [Pirmez and Imran, 2003]. However, from Figure 1, it is noted that experimental data, as fitted by bed roughness and flow Froude number [Keevil *et al.*, 2006; Amos *et al.*, 2010], do not always agree with the secondary flow behavior predicted by Abad *et al.* [2011].

[5] In this paper, we elucidate the model assumptions made in prior studies and highlight their importance, enabling a holistic model of secondary flow to be developed for submarine channels. We make three refinements to the approach of Abad *et al.* [2011] to clarify the physical

conditions favoring the onset of either river-reversed or river-normal flows:

[6] *Refinement of radial stratification*: Previous studies of the fundamental physical processes controlling secondary flow structure have either considered unstratified [Corney *et al.*, 2006] or vertically stratified flow density [Abad *et al.*, 2011]. In this study, we highlight how radial variations in depth-averaged density result in baroclinic pressure gradients that may have a significant impact on the radial flow structure, as is also often the case in stratified estuarine environments [Dyer, 1973; Fischer, 1976; Dyer, 1989; Chant and Wilson, 1997; Nidzieko *et al.*, 2009]. Whilst numerical flow models [Giorgio Serchi *et al.*, 2011; Huang *et al.*, 2012] have implicitly incorporated these effects, in this paper we highlight for the first time their significance in the generation of river-reversed or river-normal flow.

[7] *Inclusion of Coriolis forcing*: A limitation of prior studies [Corney *et al.*, 2006; Imran *et al.*, 2007; Abad *et al.*, 2011; Giorgio Serchi *et al.*, 2011] is that, in adopting the classical “Rozovskiiian” approach, they neglect Coriolis effects. Yet at high latitude, Coriolis forcing is potentially an important influence on secondary flows because (i) it contributes to the imbalance between the cross-channel centrifugal and pressure-gradient forces that drive secondary flows in meander bends [e.g., Komar, 1969; Klaucke *et al.*, 1997, 1998] and (ii) it enhances or suppresses the superelevation of transverse flow profiles [e.g., Davies *et al.*, 2006; Wells, 2009; Cossu and Wells, 2010; Cossu *et al.*, 2010]. In this study, we address this limitation by investigating how Coriolis forces may reverse the orientation of near bed flow or enhance flow superelevation, as suggested by Cossu and Wells [2010, 2013] and Peakall *et al.* [2012].

[8] *Selection of boundary conditions*: Given the above refinements to the Rozovskii-Corney-Abad (RCA) framework for radial flow within a submarine meander, the radial

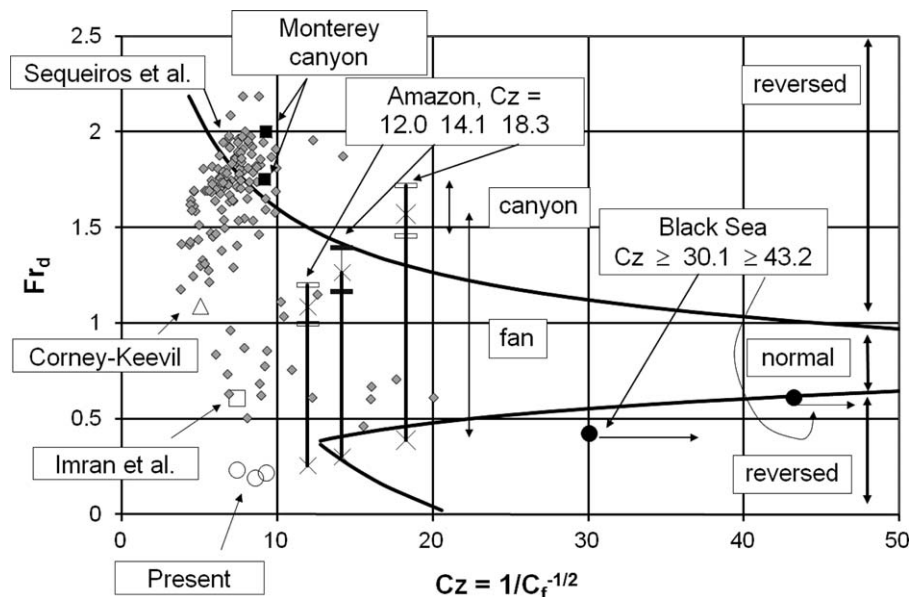


Figure 1. Plot of the Abad *et al.* [2011] transitional river-reversed and river-normal submarine meander flow phase space, plotted as a function of densimetric Froude number (Fr_d) versus Chezy drag coefficient (C_z), reproduced from Figure 25 of Abad *et al.* [2011].

flux boundary conditions used to close the flow model are carefully reconstructed. Boundary conditions describing the magnitude of convective transport terms are shown to be of critical importance when determining the secondary flow structure. Two-dimensional models refer to the classical approach of the RCA framework where radial fluxes are negligible, whereas non-negligible material fluxes arise naturally within the three-dimensional flow framework postulated herein.

[9] The above refinements to the RCA framework for radial flow allow further interpretation of the key physical processes driving river-reversed flow within submarine channels. With reference to previous experimental research [Corney *et al.*, 2006; Abad *et al.*, 2011], we show that a three-dimensional framework, as considered implicitly by Giorgio Serchi *et al.* [2011] and Huang *et al.* [2012], is necessary to accurately predict the radial flow structure. Development of the two-dimensional RCA framework into a three-dimensional framework enables us to produce new phase-space diagrams that illustrate the environmental conditions, including a near-bed downstream flow velocity maximum and outer bank-oriented net radial material transport or Coriolis forcing, that favor river-reversed versus river-normal secondary flows. The model that we develop in this paper represents the first time that the balance of Coriolis, hydrostatic, and centrifugal forces within a submarine flow has been systematically investigated in a theoretical framework. Our analysis also reveals the significance of three-dimensional flow effects on the orientation of near bed flow. We highlight that, within a bounded channel, a three-dimensional flow framework, incorporating hydrostatic forces, Coriolis forces, and flow baroclinicity, is required to accurately model the radial structure of secondary flow within submarine meanders.

2. Physical Model for Secondary Flow Within a Subaerial or Submarine Meander

[10] In this section, the classical Rozovskiian model of secondary flow within a meandering fluvial system is outlined. The model is then rendered into dimensionless form,

and parameters describing downstream flow velocity and vertical stratification are introduced.

2.1. The Rozovskiian Flow Model

[11] Standard analysis of an incompressible fluid flow across slowly varying topography, such as subaerial and submarine meanders, assumes that horizontal length scales (L , given here by the radius of curvature of the flow) are much greater than vertical length scales (given here as h , the flow depth). Through dimensional analysis, considering $\delta = h/L \ll 1$, the Reynolds averaged mass and momentum conservation equations for fluid flow can be expressed in a simplified state, henceforth referred to as the shallow water equations. As first discussed by Rozovskii [1957], the transverse (radial) component of flow, u_r , and the gauge pressure, P , within a meander can be determined from the leading order shallow water momentum conservation equations so long as the flow’s downstream (rotational) velocity, u_θ , is known a priori

$$\frac{\partial}{\partial z} \nu_t \frac{\partial u_r}{\partial z} = \frac{1}{\rho_a} \frac{\partial P}{\partial r} - fu_\theta - \frac{u_\theta^2}{r}$$

turbulent shear stress
radial pressure gradient
Coriolis force
centrifugal force

(1)

$$-G = \frac{1}{\rho_a} \frac{\partial P}{\partial z}$$

gravitational acceleration
vertical pressure gradient

(2)

[12] In (1), the turbulent shear stress term, parameterized by the eddy viscosity, ν_t , multiplied by the vertical gradient of the transverse velocity, is balanced by the Coriolis force, the radial pressure gradient, and any centrifugal forces acting on the flow. Herein, the Coriolis force, f , is locally constant and given by $f = 2\omega \sin(\alpha)$, where ω denotes the angular frequency of, and α the latitude on, the spherical body (Figure 2). In (2), the vertical pressure gradient is balanced by the gravitational force acting on the flow, G , where ρ_a denotes the ambient fluid density and r is the

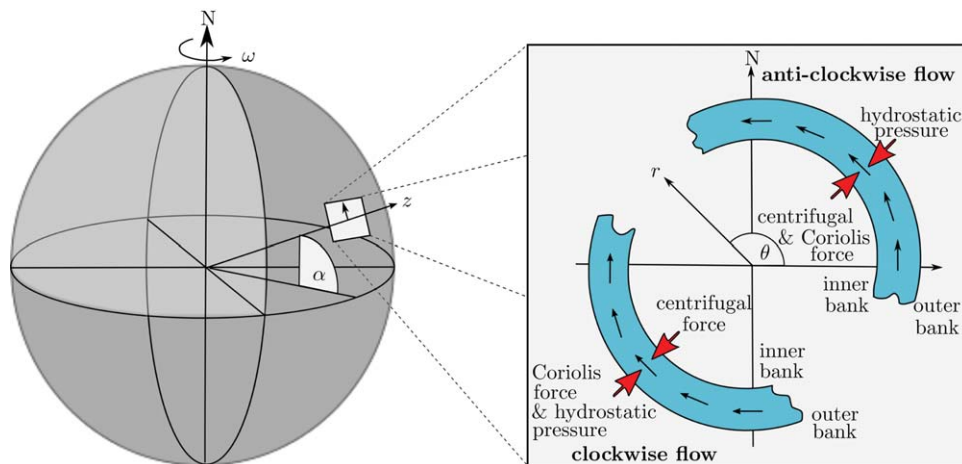


Figure 2. Orientation of forces balancing turbulent shear stress (1) in the northern hemisphere of a rotating spherical body.

radial distance across the channel. Note that, strictly speaking, additional convective acceleration terms appear within the radial momentum conservation equation (1):

$$u_r \frac{\partial u_r}{\partial r} + \frac{u_\theta}{r} \frac{\partial u_r}{\partial \theta} + u_z \frac{\partial u_r}{\partial z}, \quad (3)$$

where u_z denotes the vertical component of flow, but based on scaling arguments (see section 2.2), these terms are herein assumed to be negligible.

[13] The gravitational force acting on a density-driven submarine flow is of the form

$$G = g\phi, \quad (4)$$

in which the excess density of the flow, ϕ , compared to the ambient fluid is given by,

$$\rho_f = \rho_a + \rho_a \phi, \quad (5)$$

with ρ_f being the density of the flow and ρ_a the density of the ambient fluid. *Chernetsky et al.* [2010] assumed that density is linearly proportional to salinity. This allows the ambient fluid and flow density to be determined in terms of the ambient fluid and flow salinity denoted by s_a and s_f respectively

$$\rho_a = \rho_w(1 + \beta s_a) \quad \text{and} \quad \rho_f = \rho_w(1 + \beta s_f), \quad (6)$$

where $\rho_w \approx 1000 \text{kgm}^{-3}$ is the pure water density and $\beta \approx 7.6 \times 10^{-4} \text{psu}^{-1}$, when salinity is measured in psu [*Chernetsky et al.*, 2010]. From (5) and (6), the dimensionless excess density of the flow compared to the density of the ambient fluid, ϕ , is

$$\phi = \frac{1 + \beta s_f}{1 + \beta s_a} - 1. \quad (7)$$

[14] Under the Boussinesq approximation, $\rho_a \phi / \rho_f \ll 1$, the convective transport terms comprising the mass conservation equations are

$$\begin{array}{ccc} \frac{1}{r} \frac{\partial u_r}{\partial r} & + & \frac{1}{r} \frac{\partial u_\theta}{\partial \theta} & + & \frac{\partial u_z}{\partial z} & = & 0, \\ \text{radial fluid} & & \text{rotational fluid} & & \text{vertical fluid} & & \\ \text{transport} & & \text{transport} & & \text{transport} & & \end{array} \quad (8)$$

$$\begin{array}{ccc} \frac{1}{r} \frac{\partial u_r \phi}{\partial r} & + & \frac{1}{r} \frac{\partial u_\theta \phi}{\partial \theta} & + & \frac{\partial u_z \phi}{\partial z} & = & 0, \\ \text{radial density} & & \text{rotational density} & & \text{vertical density} & & \\ \text{transport} & & \text{transport} & & \text{transport} & & \end{array} \quad (9)$$

and are used to close the momentum conservation equation (17). In this paper, it is assumed for simplicity that diffusion of the saline solution, as discussed by *Herbert et al.* [1988], is negligible in comparison to advective fluxes.

[15] The dimensionless excess density, ϕ , may be expressed in terms of the depth-averaged dimensionless excess density, $\bar{\phi}$, multiplied by a stratification function ϕ , such that:

[16] For submarine flows, *Abad et al.* [2011] discussed the importance of vertical stratification on secondary flow field structure, but they implicitly assumed that the radial derivative of $\bar{\phi}$ is negligible. Whilst field evidence of the effect of flow baroclinicity in submarine channels is not available, it is well established as a driving force in comparable, highly stratified, estuarine systems [*Dyer*, 1973; *Chant and Wilson*, 1997; *Lacy and Monismith*, 2001]. Further evidence for the significance of the radial variation of the depth-averaged flow density is found in the numerical studies of *Imran et al.* [2004], *Kassem and Imran* [2004], and *Giorgio Serchi et al.* [2011]. For these reasons, the effect of the radial and rotational variation of hydrodynamic flow properties, including depth-averaged dimensionless excess density, $\bar{\phi}$, on the secondary flow structure is explicitly analyzed and discussed in this paper. Following *Abad et al.* [2011], we assume that, within a submarine meander, the interface between the flow and ambient fluid is well defined, that entrainment of ambient fluid from above may be neglected and that the stratification function ϕ may be normalized such that $\int_0^\infty \phi dz = h$ [*Parker et al.*, 1987; *Sequeiros et al.*, 2010]. Thus, assuming that the flow is radially and vertically stratified, the flow pressure is given by

$$P = \rho_a g \bar{\phi}(r) \int_z^\infty \phi(z', r) dz'. \quad (11)$$

[17] From (11), the pressure gradient is therefore

$$\begin{aligned} \frac{1}{\rho_a} \frac{\partial P}{\partial r} &= g \bar{\phi} \frac{\partial h}{\partial r} \left(\int_\eta^\infty \phi d\eta' + \eta \phi \right) \\ &+ gh \left(\frac{\partial \bar{\phi}}{\partial r} \int_\eta^\infty \phi d\eta' + \bar{\phi} \int_\eta^\infty \frac{\partial \phi}{\partial r} d\eta' \right) \end{aligned} \quad (12)$$

where η is the dimensionless flow depth ($\eta = z/h$) and prime notation denotes dummy integration variables. Without resolving the full three-dimensional structure of the flow, the radial variation of the flow stratification function cannot be computed. Hence, for simplicity, it is assumed that the radial gradient of the structure function ($\partial \phi / \partial r$) is negligible in comparison to the radial gradients of flow depth and depth-averaged density,

$$h \bar{\phi} \int_\eta^\infty \frac{\partial \phi}{\partial r} d\eta' \ll \bar{\phi} \frac{\partial h}{\partial r} \left(\int_\eta^\infty \phi d\eta' + \eta \phi \right), \quad h \frac{\partial \bar{\phi}}{\partial r} \int_\eta^\infty \phi d\eta', \quad (13)$$

and thus, it is assumed that the flow baroclinicity is well described by the radial depth-averaged density gradient. In this paper, the radial pressure gradient is expressed, to leading order, in terms of the transverse slope of the interface and transverse density gradient:

$$\begin{aligned} \frac{1}{\rho_a} \frac{\partial P}{\partial r} &= g \bar{\phi}(r) \frac{\partial h}{\partial r}(r) \left(\int_\eta^\infty \phi(\eta', r) d\eta' + \eta \phi(\eta) \right) \\ &+ gh(r) \frac{\partial \bar{\phi}}{\partial r}(r) \int_\eta^\infty \phi(\eta', r) d\eta'. \end{aligned} \quad (14)$$

2.2. Dimensionless Flow Variables

[18] To simplify (1) and (2), we express them in terms of a series of dimensionless parameters. In (1), the eddy

viscosity is assumed to be vertically constant. This simplistic approach still captures fundamental physical processes [Dorrell and Hogg, 2012] and is consistent with prior studies [Rozovskii, 1957; Corney et al., 2006; Abad et al., 2011]. In what follows the Chezy drag function used to model the basal shear stress is characterized in terms of a bed roughness height, $z_0 \ll h$. Using the flow length scales, eddy viscosity, ν_t , and depth-averaged downstream flow velocity, \bar{u}_θ , the flow variables are given in terms of dimensionless parameters, denoted by the use of capitals, as

$$\left. \begin{aligned} r &= LR, & z_0 &= h\eta_0, \\ u_r &= \delta\bar{u}_\theta ReU_r, & u_z &= \delta^2\bar{u}_\theta ReU_z, \\ 2L\omega \sin(\alpha) &= \bar{u}_\theta Ro^{-1}, & \frac{\partial h}{\partial r} &= \delta Fr_d^2 \mathcal{S}, \\ h \frac{\partial \bar{\phi}}{\partial r} &= \delta \bar{\phi} Fr_d^2 \mathcal{G}, & u_\theta &= \bar{u}_\theta U_\theta \end{aligned} \right\}, \quad (15)$$

where $Re = h\bar{u}_\theta/\nu_t$ is the depth-averaged Reynolds number of the flow. Thus, the convective acceleration terms (3) now become

$$\delta Re \frac{\bar{u}_\theta^2}{L} \left(\delta Re U_r \frac{\partial U_r}{\partial R} + \frac{U_\theta}{R} \frac{\partial U_R}{\partial \theta} + \delta Re U_z \frac{\partial U_r}{\partial \eta} \right). \quad (16)$$

[19] Since we have assumed that the flow aspect ratio $\delta \ll Re^{-1}$, it follows that the convective acceleration terms (16) are negligible.

[20] Equation (15) gives the Rossby number as the ratio of inertial to Coriolis force; the sign of the Rossby number is therefore a function of latitude and of the rotational direction of the flow, with clockwise flow negative and anticlockwise flow positive (Figure 2). Minimal values of the Rossby number, of order 0.1, may occur in large bends located at high latitudes [Peakall et al., 2013], and maximal values of the Rossby number will occur near the equator as $f \rightarrow 0$. Furthermore, the densimetric Froude number, Fr_d , denotes the ratio of inertial to gravitational forces $Fr_d = \bar{u}_\theta / \sqrt{g\bar{\phi}h}$. Henceforth, the dimensionless radial derivative of the flow depth, \mathcal{S} , will be referred to as the normalized transverse water slope. Likewise, the dimensionless radial derivative of $\bar{\phi}$, \mathcal{G} , will be referred to as the normalized transverse density gradient. Thus, from (1) and (15), the radial component of flow, along a curve of constant radius $r=L$, is expressed as a second order, dimensionless, ordinary differential equation:

$$\frac{\partial^2 U_r}{\partial \eta^2} = \mathcal{S}f_1 + \mathcal{G}f_2 - Ro^{-1}U_\theta - U_\theta^2$$

turbulent	normalized	normalized	Coriolis	centrifugal
shear	water	density	force	force
stress	slope	gradient		

(17)

where, from (14), the structure functions f_1 and f_2 describe hydrodynamic pressure as

$$f_1 = \int_\eta^\infty \varphi d\eta' + \eta\varphi \quad \text{and} \quad f_2 = \int_\eta^\infty \varphi d\eta'. \quad (18)$$

2.3. Empirical Structure Functions for the Vertical Density Stratification and Downstream Flow Velocity

[21] To solve equation (17), it is necessary to know, a priori, the normalized vertical velocity and density profiles. Here we use the empirical formulation of Abad et al. [2011] for the dimensionless depth-averaged downstream velocity, U_θ ,

$$U_\theta = \frac{T_p}{\int_0^1 T_p d\eta}, \quad (19)$$

such that $\int_0^1 U_\theta d\eta = 1$ and the structure function T_p is given by

$$T_p = \begin{cases} \frac{\chi + \eta - \frac{1}{2}\eta^2}{\chi + \eta_1 - \frac{1}{2}\eta_1^2} & 0 \leq \eta \leq \eta_1 \\ \frac{1 - \eta}{1 - \eta_1} & \eta_1 < \eta \leq 1 \end{cases}, \quad (20)$$

where η_1 is the dimensionless depth of the downstream flow velocity maximum and $\eta = 1$ denotes the flow-ambient fluid interface. Abad et al. [2011] proposed that η_1 may be expressed as a function of the densimetric Froude number

$$\eta_1 = 0.8 - 0.27Fr_d, \quad (21)$$

for $0.19 \leq Fr_d \leq 2.21$. From Engelund [1974] and Soulsby [1997], the slip parameter, χ , may be given in terms of a bed roughness length scale, η_0 , or a Chezy drag coefficient C_z ,

$$\left(\frac{0.077}{\chi + \frac{1}{3}} \right)^2 = 0.0474\eta_0^{\frac{1}{3}} = \frac{1}{C_z^2}. \quad (22)$$

[22] The stratification of the submarine flow, ϕ , is given in terms of the depth-averaged dimensionless excess density, $\bar{\phi}$, multiplied by a density structure function, ϕ , (10). Simplistic ‘‘top-hat’’ models impose zero stratification of the fluid density [Parker et al., 1986],

$$\varphi = 1. \quad (23)$$

[23] However, Sequeiros et al. [2010] and Abad et al. [2011] suggested that such simplistic models do not accurately describe the hydrostatic pressure field, and hence the radial pressure gradient, with Abad et al. [2011] proposing an alternative stratification function, f_s ,

$$\varphi = \frac{f_s}{\int_0^1 f_s d\eta}. \quad (24)$$

[24] Indeed, Abad et al. [2011] proposed a nonuniform stratification function of the form

$$f_s = \begin{cases} 1 & \eta_2 < 1 \\ \begin{cases} 1 & \eta \leq \eta_2 \\ 1 - \frac{\eta - \eta_2}{1 - \eta_2} & \eta > \eta_2 \end{cases} & \eta_2 < 1, \end{cases} \quad (25)$$

where the depth η_2 is related to the depth of the maximum velocity, η_1 , using:

$$\eta_2 = 2.59 \exp\left(-2.5 \frac{0.8 - \eta_1}{0.27}\right). \quad (26)$$

[25] Note that, if $\eta_2 \geq 1$ (i.e., for $\eta_1 > 0.7$), the density profile of the flow is vertically uniform.

[26] In Figure 3, the principal forces affecting the orientation of radial flow (17) are plotted based on the vertical velocity (20) and density stratification functions (25). It is seen that the magnitude and vertical structure of the centrifugal, and to a lesser extent the Coriolis, forces are dependent on the depth of the velocity maximum, η_1 , and the bed roughness height, η_0 . Figure 3a shows that near bed centrifugal forces increase as either η_1 or η_0 are decreased. Figure 3b shows that the Coriolis force is primarily dependent on the magnitude and sign of the Rossby number, recalling (2) that outer-bank oriented, positive Rossby number forcing is associated with anticlockwise flow in the northern hemisphere or clockwise flow in the southern hemisphere. Figures 3c and 3d highlight that the radial pressure gradient (14) is primarily determined by the magnitude and orientation of the normalized transverse water slope and normalized transverse density gradient.

3. Boundary Conditions and Radial Flow Structure

[27] The radial component of secondary flow (1) is solved subject to basal and flow-ambient fluid interface boundary conditions and mass continuity conserving flux conditions. Along with the structure functions describing the vertical variation of downstream flow velocity and the density stratification, we use these boundary conditions to

define four radial flow models (Table 1) that are analyzed in further detail in sections 4 and 5.

[28] The slip velocity model of *Engelund* [1974] is closed using a boundary condition to model bed resistance, where

$$U_r = \chi \frac{\partial U_r}{\partial \eta} \Big|_{\eta=0}, \quad (27)$$

and the slip parameter χ is determined in terms of the bed roughness height, η_0 (22). *Soulsby* [1997] gives the dimensionless roughness height in terms of the median grain size of the bed material, d_{50} ,

$$\eta_0 = \frac{d_{50}}{12h}, \quad (28)$$

where it is assumed that bedforms have a negligible impact on the flow.

[29] Attempts have been made to model some of the physical processes operating at the flow-ambient interface, e.g., entrainment of ambient fluid [*Parker et al.*, 1987]. However, the turbulent nature of fluid flow means that the exact location and behavior of a nominal flow-ambient fluid is poorly constrained. For consistency with the downstream flow model of *Abad et al.* [2011], where $u_\theta = 0$ at $\eta = 1$ (20), we assume that the transverse velocity at the interface between the density current and the ambient fluid is also zero, such that:

$$U_r = 0|_{\eta=1}. \quad (29)$$

[30] However, previous studies [*Corney et al.*, 2006; *Imran et al.*, 2007; *Abad et al.*, 2011] have defined the flow-ambient fluid interface using an alternative boundary

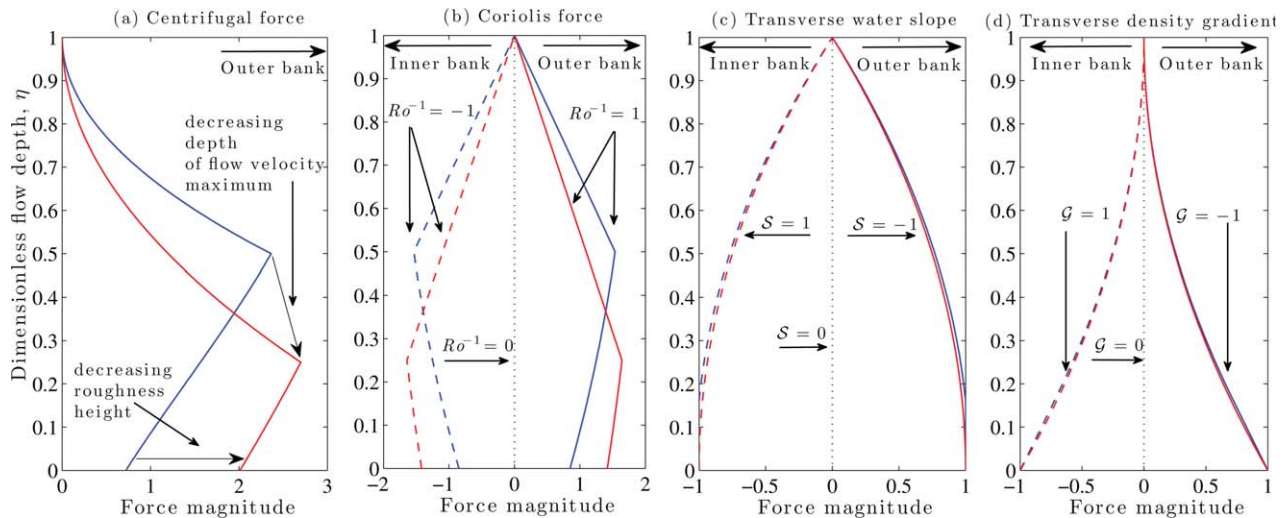


Figure 3. The orientation and magnitude of the dimensionless (a) centrifugal force, (b) Coriolis force, and forces arising from the scaled (in terms of the aspect ratio of the flow) normalized, transverse water slope (c) and transverse density gradient (d), as determined from the downstream flow velocity (20) and density stratification (25) structure functions. Red curves have a decreased flow velocity maximum and bed roughness height in comparison to blue curves. Forces acting on the flow toward the outer bank are denoted by solid curves, forces acting on the flow toward the inner bank are denoted by dashed curves, and zero forcing on the flow is denoted by dotted curves.

Table 1. Radial Flow Models 1–4

	Density Distribution	Boundary Conditions	Flow Framework
Model 1 (section 4.1, Figure 5a)	Unstratified, $\varphi = 1$ Barotropic, $\mathcal{G} = 0$	$U_r = \chi \frac{\partial U_r}{\partial \eta} _{\eta=0}$ $U_r = 0 _{\eta=1}$	Two-dimensional $Q_{rf} = 0$ $Q_{rf} = Q_{rs}$
Model 2 (section 4.2, Figure 5b)	Stratified, $\varphi \neq 1$ Barotropic, $\mathcal{G} = 0$	$U_r = \chi \frac{\partial U_r}{\partial \eta} _{\eta=0}$ $\frac{\partial U_r}{\partial \eta} = 0 _{\eta=1}$	Two-dimensional $Q_{rf} = 0$ $Q_{rf} \neq Q_{rs}$
Model 3 (section 4.3, Figure 6)	Stratified, $\varphi \neq 1$ Baroclinic, $\mathcal{G} \neq 0$	$U_r = \chi \frac{\partial U_r}{\partial \eta} _{\eta=0}$ $U_r = 0 _{\eta=1}$	Two-dimensional $Q_{rf} = 0$ $Q_{rs} = 0$
Model 4 (section 5, Figures 8 and 9)	Stratified, $\varphi \neq 1$ Baroclinic, $\mathcal{G} \neq 0$	$U_r = \chi \frac{\partial U_r}{\partial \eta} _{\eta=0}$ $U_r = 0 _{\eta=1}$	Three-dimensional $Q_{rf} \neq 0$ $Q_{rs} \neq 0$

condition of vanishing shear stress. The vanishing shear-stress condition, used in subaerial flows where the shear stress at the free surface can reasonably be assumed to vanish due to the density difference between the flow and the atmosphere, is implemented by constraining the vertical gradient of the flow velocity to be zero at $\eta = 1$:

$$\frac{\partial U_r}{\partial \eta} = 0 |_{\eta=1}. \quad (30)$$

[31] Although the boundary condition (29) used here is different from that employed in previous research (30), we argue that it is physically realistic and consistent with both the formalization of the downstream velocity profile and experimental observation (section 4.4). In the supporting information available online, the choice of flow-ambient fluid boundary condition is discussed further.

[32] In the following subsections, the mass conservation equations (8) and (9) are used to provide integral conditions to further constrain the radial flow model (17). We initially discuss classical flow models in which the flow is assumed to be rotationally constant before considering a model where the flow is not rotationally constant. For simplicity, in this paper it is assumed that $\delta Re \ll 1$ and hence the convective *acceleration* terms from the radial momentum conservation equation (16) are always be assumed to be negligible. However, as discussed in section 3.2. later, convective *transport* terms in the mass conservation equation, see (8) and (9), may still be non-negligible.

3.1. Two-Dimensional, Rotationally Constant, Models of Meander Flow

[33] Two-dimensional flow models follow the approach of *Rozovskii* [1957], where Reynolds averaged mean flow variables are assumed to be rotationally invariant, meaning that within a meander, along a radius of constant curvature, the downstream velocity and density parameters are constant. Integrating (8) and (9) over the fluid depth, the depth-integrated radial fluid flux, q_{rf} , and density flux, q_{rs} , describing the rate at which fluid and excess density is transported from the inner to outer bank or vice versa, are given by

$$q_{rf} = \int_0^\infty u_r dz = \frac{c_0}{r}, \quad (31)$$

$$q_{rs} = \int_0^\infty u_r \varphi dz = \frac{c_1}{\phi r}. \quad (32)$$

[34] Whilst the bed depth is temporally constant, as in the saline gravity currents considered in this paper, the parameters, u_z and φu_z , evaluated at $\eta = 0$ and as $\eta \rightarrow \infty$, that arise in the depth integral of (8) and (9) may be assumed to vanish. Within a bounded channel, where by definition u_r and thus $q_{rf} = 0$ at the channel walls, it is apparent from (31) that $q_{rf} = 0$ [Rozovskii, 1957]. Moreover, whilst $u_r = 0$ and thus $q_{rs} = 0$ at the channel boundaries, then $q_{rs} = 0$ across the channel width. Here it is highlighted that *Abad et al.* [2011] constrain the radial fluid flux to be zero, whilst the radial density flux is only discussed in terms of morphodynamic evolution of the bed, which is inappropriate for the nondepositional and nonerosional saline flows they considered.

[35] The radial momentum balance equation (17) is a function of the known flow depth and Coriolis force, and the unknown normalized transverse water slope, \mathcal{S} , and normalized transverse density gradient, \mathcal{G} . Within a bounded submarine channel, \mathcal{S} and \mathcal{G} are therefore implicitly constrained by the dimensionless depth-integrated fluid flux, Q_{rf} , and density flux, Q_{rs} ,

$$Q_{rf} = \int_0^\infty U_r(\eta, \mathcal{S}, \mathcal{G}) d\eta = 0, \quad (33)$$

$$Q_{rs} = \int_0^\infty U_r(\eta, \mathcal{S}, \mathcal{G}) \varphi(\eta) d\eta = 0. \quad (34)$$

[36] Thus, in conjunction with the boundary conditions (27) and (29), the depth-integrated radial fluid flux (33) and density flux (34) close the radial momentum balance equation (17). Henceforth, the fluid and the depth-integrated radial density flux conditions will be referred to as the radial material fluxes of the flow.

3.2. Three-Dimensional, Rotationally Varying, Models of Meander Flow

[37] For the more physically realistic case, where flow properties vary rotationally around a meander, the radial derivatives of the flow velocity, depth, and the depth-averaged dimensionless excess density are non-negligible. Integrating (8) and (9) over the fluid depth, it is seen that

the dimensional, depth-integrated fluid, and density fluxes are nonzero:

$$q_{rf} = -\frac{1}{r} \int_0^\infty \int_0^r \frac{\partial}{\partial \theta} u_\theta dr' dz' \Big|_{r=L, \theta=\theta_c}, \quad (35)$$

$$q_{rs} = -\frac{1}{r\phi} \int_0^\infty \int_0^r \frac{\partial}{\partial \theta} u_\theta \bar{\phi} \varphi dr' dz' \Big|_{r=L, \theta=\theta_c}, \quad (36)$$

with a magnitude dependent on the radial distance across channel, where $r=L$, and θ_c , the angle of rotation around the meander. In (35) and (36), it is assumed that the rotational derivative terms are non-negligible and thus of similar order to the radial material fluxes. This assumption implies that $\partial \bar{u}_\theta / \partial \theta$ is of order δRe and thus the depth-averaged downstream velocity is rotationally constant to leading order. The dimensionless forms of the radial fluid flux and the depth-integrated radial density flux, used to close (17), thus take the form,

$$Q_{rf} = \int_0^\infty U_r d\eta = \frac{1}{\delta h \bar{u}_\theta Re} q_{rf} \Big|_{r=L, \theta=\theta_c}, \quad (37)$$

$$Q_{rs} = \int_0^\infty U_r \varphi d\eta = \frac{1}{\delta h \bar{u}_\theta Re} q_{rs} \Big|_{r=L, \theta=\theta_c} \quad (38)$$

[38] Nonzero radial material fluxes correspond to a net transport of material across the channel. This implies that, on a curve of constant radius, the downstream flux of material varies around the meander bend. The radial fluid flux and the net change in flow density are nonzero when closed

within a three-dimensional flow framework, due to fluxes of material entering from upstream and exiting downstream [Dietrich and Whiting, 1989; Nelson and Smith, 1989]. Moreover, such net material transport may be enhanced through topographic forcing such as point bars and scours [Peakall et al., 2007], flow overspill [Keevil et al., 2007; Janocko et al., 2013], superelevation of the flow [Pirmez and Imran, 2003], and progression of the velocity maximum core toward the outer bank [Imran et al., 1999]. In section 3.3, the plausible vertical structure of the radial component of secondary flow will be discussed, based on the governing equation (17), the velocity and density stratification profiles (see section 2.3), and the flow boundary conditions discussed above.

3.3. The Structure of the Radial Component of Secondary Flow Within a Submarine Meander

[39] Given the downstream velocity profile (20) and vertical density stratification (24), the radial component of secondary flow, U_r , may be found by integrating the flow field equation (17). From the boundary conditions discussed in sections 3.1 and 3.2, the theoretical solution for U_r can be constrained to one of the six possible types (Figure 4). Figure 4 shows that these various radial flow structures may be distinguished with reference to subaerial river-normal flows, which consist of a single helical cell with near-bed radial flow directed toward the inner bank (Figure 4b). In contrast, if the near bed flow is directed toward the outer bank, the secondary flow is denoted as river-reversed (Figure 4e).

[40] More complex secondary flow structures also exist, where multiple helical cells are stacked upon each other.

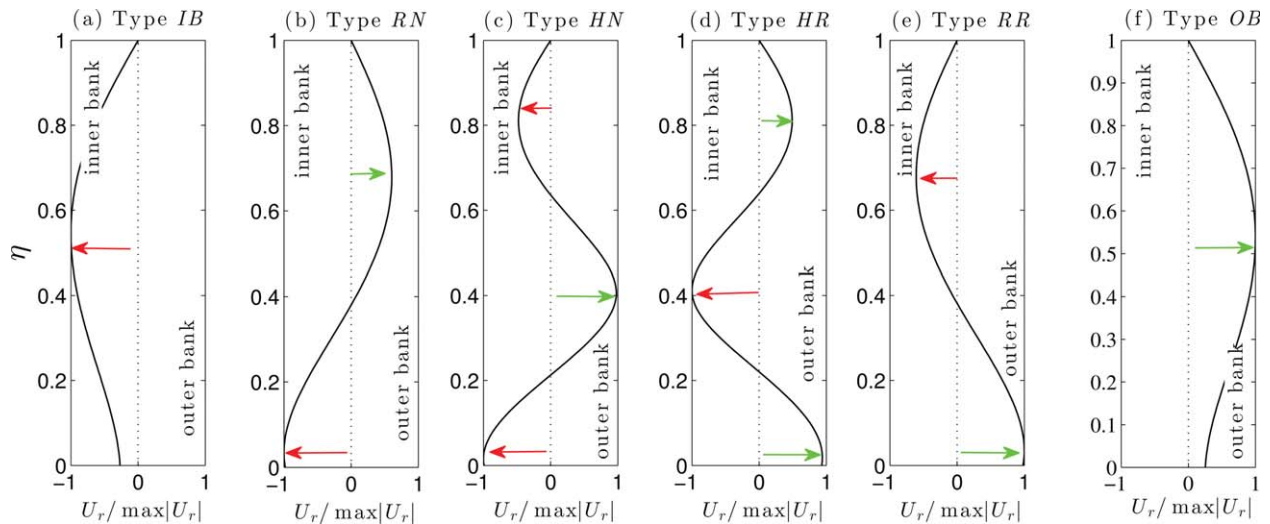


Figure 4. Classification of the radial component of secondary flow structure within submarine meanders (a)–(f), as distinguished by comparison of the vertical flow structure U_r to classical subaerial meander flow. Black curves denote normalized flow velocity, and red arrows denote inner and green arrows outer bank flow orientation. (a) Type *IB* denotes flow directed toward the inner bank. (b) Type *RN* denotes meander normal flow consisting of a single helical cell. (c) Type *HN* secondary flow consisting of multiple helical cells, with near bed flow toward the inner bank. (d) Type *HR* also consists of multiple helical cells but has near bed flow oriented toward the outer bank. (e) Type *RR* denotes meander reversed flow, where the near bed flow is toward the outer bank. (f) Type *OB* denotes flow directed toward the outer bank.

Helical couplets of two [Imran *et al.*, 2007] or more [Rozovskii, 1957] complete cells can form, depending on flow and morphological conditions. We distinguish these stacked helical cells by reference to the behavior of the radial flow near the bed (Figure 4). If the radial component of near-bed secondary flow is directed toward the inner bank, then solutions with multiple cells are defined as river-normal (*HN*; Figure 4c). Conversely, if the radial component of the near-bed secondary flow is directed toward the outer bank, the helical cell solutions are denoted as river-reversed (*HR*; Figure 4d). For completeness, we also define categories of secondary flow in which the radial flow throughout the entire vertical depth may be oriented either toward the inner (*IB*; Figure 4a) or outer banks (*OB*; Figure 4f), respectively.

[41] In sections 4 and 5, these radial flow structures are determined as a function of the material fluxes, Q_{rs} and Q_{rf} , which implicitly constrain the transverse water slope and density gradient, the dimensionless depth of the velocity maximum, η_1 , and bed roughness height, η_0 , and the Coriolis forcing, herein described by the inverse Rossby number Ro^{-1} . Note that we focus on the dimensionless depth of the velocity maximum, η_1 , a departure from the use of the bulk Froude number in the study by Abad *et al.* [2011]. In reality, η_1 can be related to the Froude number via (21), but we prefer to use η_1 in that it can be more readily and explicitly related to changes in the distribution and magnitude of centrifugal forces [Corney *et al.*, 2008], see Figure 3a.

4. Two-Dimensional Flow Framework Models of Secondary Circulation Within Bounded Submarine Meanders

[42] In this section, we discuss the radial structure of secondary flow as derived using models 1–3 (Table 1). Through comparison against the simplest, unstratified flow model (section 4.1), it is shown that predicted flow dynamics vary significantly with the introduction of flow stratification (section 4.2) and baroclinic effects (section 4.3). Moreover, through comparison against previous experimental research, we show that the two-dimensional closure favored in prior studies [see section 3.1; Corney *et al.*, 2006; Abad *et al.*, 2011] is insufficient to model submarine flow dynamics (sections 4.3 and 4.4).

4.1. Two-Dimensional, Unstratified, Barotropic Meander Flow Models

[43] The simplest force balance model (model 1) of radial flow (17) assumes that the flow density is unstratified, as per standard top-hat models of saline density currents [Parker *et al.*, 1986]. The radial fluid flux and the depth-integrated radial density flux are by definition equivalent; thus, there are insufficient flux boundary conditions to constrain both the normalized transverse water and density gradients. Therefore, it is assumed that the flow is barotropic such that the normalized radial density gradient, \mathcal{G} , is zero (Table 1), meaning (17) may be simplified to yield:

$$\frac{\partial^2 U_r}{\partial \eta^2} + Ro^{-1} U_\theta - \mathcal{S}f_1 + U_\theta^2 = 0. \quad (39)$$

[44] Equation (39) is solved subject to the boundary conditions (27) and (29), with the normalized transverse water

slope \mathcal{S} being determined from the radial flux condition, $Q_{rf} = Q_{rs} = 0$, (33) and (34).

[45] Bed roughness may be expressed by either a dimensionless roughness length scale, η_0 , or Chezy drag coefficient, C_z , (Figure 5a) as per prior studies [see, e.g., Komar, 1970; Ren *et al.*, 1996; Umlauf and Arneborg, 2009; Darby and Peakall, 2012]. Here it is noted that the smoother the flow bed, the greater the near-bed centrifugal force (Figure 3a), and therefore, the more likely it is that the flow is river-reversed. However, if the downstream flow velocity maximum, η_1 , is near the flow-ambient fluid interface, centrifugal forces dominate over the radial pressure gradient forces near the interface, driving outer bank-oriented near-interface secondary flow. In contrast, near the bed, the secondary flow is directed toward the inner bank. However, if the downstream flow velocity maximum is located near the bed, the dominant centrifugal forces drive near-bed flow toward the outer bank. Thus, Figure 5a shows that, by decreasing either η_1 or η_0 , the flow undergoes a transition from river-normal (*RN*; Figure 4b) to river-reversed (*RR*; Figure 4e) flow, via the generation of multiple helical cells with inner bank-oriented near-bed flow (*HN*; Figure 4c).

4.2. Two-Dimensional, Vertically Stratified, Barotropic Meander Flow Models: Comparison to the Research of Abad *et al.* [2011]

[46] Whilst model 1 describes an unstratified, barotropic flow, it does not accurately represent flow stratification present in submarine density currents [Peakall *et al.*, 2000; Abad *et al.*, 2011; Giorgio Serchi *et al.*, 2011]. To elucidate the impact of vertical density stratification on submarine meander flow dynamics, we compare the unstratified model 1 to the stratified model 2 (i.e., the model of Abad *et al.* [2011]). Model 2 specifies a vertical stratification of the flow density using the structure function described in (25). Here we specify a zero fluid flux condition to close the model (33), coupled with the slip velocity condition (27) and a vanishing shear stress interface condition (30), following Abad *et al.* [2011], as discussed earlier.

[47] In Figure 5b, it can be seen that the results of Abad *et al.* [2011] are replicated, though here the river-normal flows are further divided into single-cell and two-cell structures (Figure 5b, *DEF*). However, we note that in the stratified flow model 2, river-reversed flow is constrained to a smaller range of flow conditions than in the unstratified flow model 1. This is the result of stratified flow reducing the radial pressure gradient near the flow-ambient fluid interface, enhancing outer bank-oriented near interface flow and inner bank (river-normal)-oriented near bed flow. The localized region of meander reversed (*ABC*) flow matches that in Abad *et al.* [2011]. The formation of such transitional regions (Figure 5b, *ABC* and *DEF*) is caused by flow stratification-induced variations in the force balance equation (17). Moreover, it is noted that, whilst the fluid flux in model 2 is constrained to be zero [Abad *et al.*, 2011], the density flux is unconstrained and therefore may be nonzero. In the following section, we address this weakness through a stratified flow model where both material flux conditions are constrained to be zero to satisfy the mass conservation conditions (33) and (34) (model 3; see Table 1).

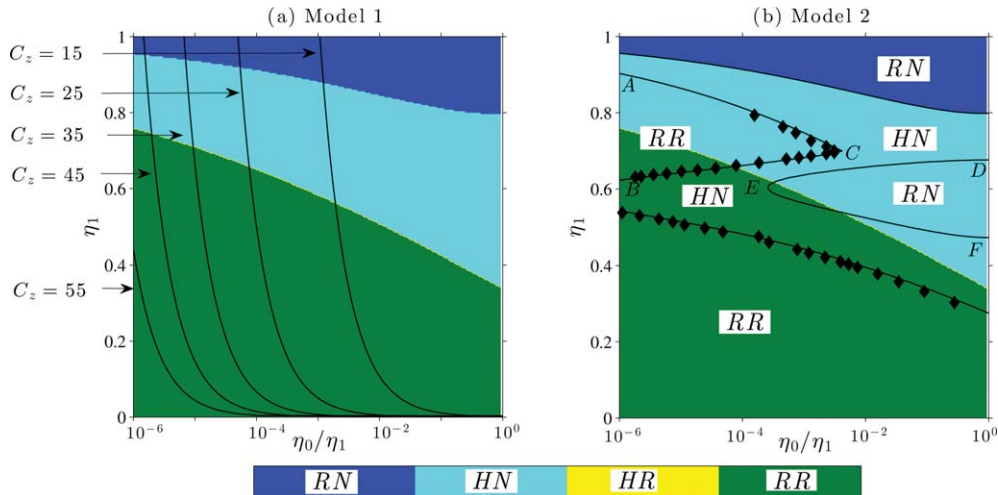


Figure 5. (a) The variation of the vertical structure of radial flow within a submarine meander as a function of the depth of the flow velocity maximum, η_1 , and flow roughness height, η_0 , for the unstratified flow model 1, where black lines denote contours of constant Chezy drag coefficient C_z (22). (b) A comparison of the unstratified, radial flow model 1 (depicted by solid colors) against the stratified radial flow model (model 2) (depicted by contour lines and labels), where localized areas of meander reversed and meander normal flow are denoted by *ABC* and *DEF*, respectively. Points describing the transition in flow state plotted in Figure 24 of *Abad et al.* [2011] are replotted here, as denoted by black markers. η_1 denotes the dimensionless depth of the velocity maximum and η_0 the dimensionless bed roughness height. The vertical structure is separated into distinct classes, see Figure 4 for information.

4.3. Two-Dimensional, Baroclinic, Meander Flow Models

[48] In this section, the solutions for radially stratified flows are discussed subject to appropriate zero material flux conditions (model 3; Table 1); these flux conditions are, within a bounded channel, required to ensure conservation of mass. The radial flow structure is thus a function of the dimensionless depth of the flow velocity maximum, η_1 , roughness height η_0 , and Coriolis forcing. Moreover, unlike models 1 and 2, it is now assumed that the flow is baroclinic (i.e., the flow is radially stratified).

[49] In model 3, the governing equation is closed by the bed and interface boundary conditions (27) and (29), as well as the zero material flux conditions (33) and (34), see Table 1. However, it is noted that if the flow is unstratified (i.e., in the region $\eta_1 > 0.7$, see section 2.3), the material flux conditions (33) and (34) are identical. Thus, we restrict the solutions of model 3, as plotted in Figure 6, to regimes in which the flow is stratified, $\eta_1 < 0.7$, and four distinct boundary and flux conditions exist to close the flow model.

[50] Initially, neglecting Coriolis forces ($Ro^{-1} = 0$), model 3 predicts a radial flow regime composed of multiple helical cells, with inner bank-oriented near bed flow (Figure 6b). This is distinct from flow models 1 and 2, where the radial flow structure was shown to be strongly dependent on the dimensionless depth of the flow velocity maximum and the normalized bed roughness height (Figure 5). This does not agree with experimental results, for instance, those of *Keevil et al.* [2006, 2007]. To explain the prevalence of the inner bank-oriented near bed flow in model 3, we decompose the structure of the radial component of the flow into three regions, as depicted in Figure 7: (I) a near-bed layer where excess density flow is high; (II) an interior

layer within the flow, where excess density is still high and the flow is oriented toward a given bank; (III) a near-interface layer where the excess density of the flow vanishes. Whilst the flow is strongly stratified, $\eta_1 \ll 0.7$ (35), the near interface layer, *III*, makes a negligible contribution to the depth-integrated radial density flux. The near-bed layer of the flow, *I*, is thus oriented toward the opposite bank of the interior layer, *II*, such that the depth-integrated radial density flux is constrained to be zero. The process of constraining the depth-integrated radial density flux forces the generation of multiple helical cells with near bed flow oriented toward the inner bank (i.e., the flow regime *HN* of Figure 4c). As stratification effects become negligible ($\eta_1 \rightarrow 0.7$), the contribution to the depth-integrated radial density flux from the near interface layer becomes significant. Thus, the area (around $\eta = \eta_1$) where centrifugal forces dominate the radial pressure gradient results in the radial flow being driven toward the inner bank, generating *HN* flow in the same manner as in model (1; see Figure 5a).

[51] Model 3 is also evaluated subject to cases where the Coriolis force is directed toward the inner bank ($Ro^{-1} = -10$; Figure 6a) and outer bank ($Ro^{-1} = 10$; Figure 6c). However, the orientation of the near bed flow, forced by the radial density flux condition, is counterintuitive and does not agree with prior experimental studies [*Cossu and Wells*, 2010, 2013]. Thus, by introducing a more complete description of the flow dynamics, within a two-dimensional flow framework, the accuracy of the model is decreased. The validity of the two-dimensional flow framework is further investigated in section 4.4 by comparing the results of models 1 and 3 with the experimental results of *Corney et al.* [2006]. Model 2 is not used in this analysis, because it does

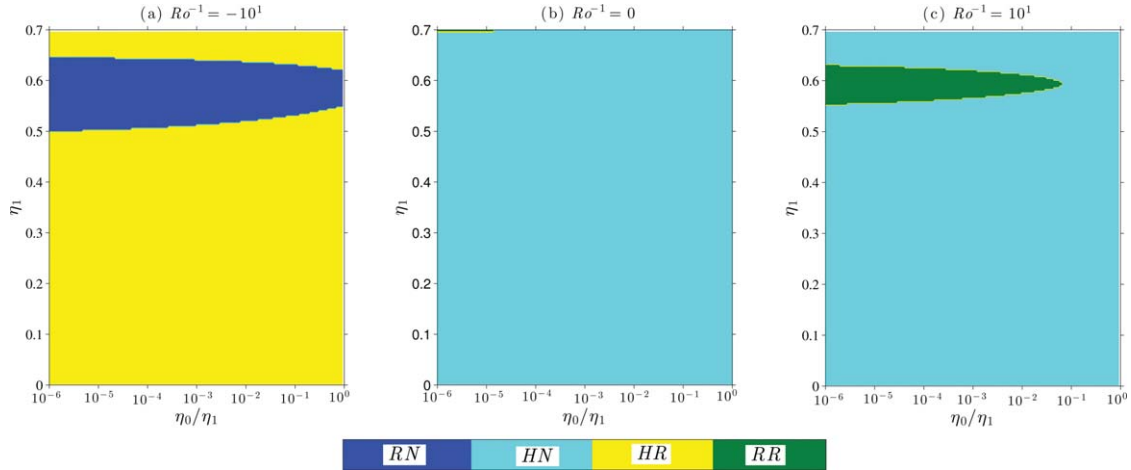


Figure 6. The structure of radial flow within a submarine meander, model 3, as a function of dimensionless depth of the flow velocity maximum, η_1 , flow roughness height, η_0/η_1 and Coriolis forcing as characterized by the inverse flow Rossby number, Ro^{-1} . The vertical structure is separated into distinct classes, see Figure 4. The stratified flow model of *Abad et al.* [2011] (25) is used to model the hydrostatic pressure within the momentum conservation equation (17) and is solved subject to a zero fluid flux depth-integrated radial density flux conditions, $Q_{rf} = Q_{rs} = 0$.

not satisfy the material flux conditions for flows modeled in a two-dimensional flow framework.

4.4. Comparison of Models 1 and 3 to the Experiments of Corney et al. [2006]

[52] In Figure 7, the radial flow models 1 and 3 are compared to the experimental data of *Corney et al.* [2006]. It is seen that neither model 1 nor model 3 can accurately capture the entire vertical structure of the radial flow observed in these experiments. Specifically, whilst the stratified flow model 3 captures the radial flow behavior well, at least near the free surface, it fails to replicate the observations closer to the base of the flow. In contrast, the near bed radial flow behavior is replicated well by the unstratified flow model 1, discussed in section 4.1. These findings might suggest that the stratification model (35) poorly captures the density distribution within the flow. Such an examination of the stratification model is beyond the scope of the current paper, though we note the importance of further research into flow structure functions to help elucidate fundamental flow processes. Whilst improved stratification functions may be developed, the underpinning theory laid out in this paper will remain the same.

[53] In the stratified flow model, the orientation of near-bed flow is controlled by the zero material flux conditions. These conditions arise from the key assumption employed in the two-dimensional framework, namely that transport of flow and material in solution or suspension is conserved within a radial slice of the flow. In the following section, we consider the implications that arise from relaxing this assumption on the predicted radial flow structure.

5. Three-Dimensional Flow Framework Models of Secondary Circulation Within Submarine Meanders

[54] As highlighted in section 3.2, within a three-dimensional flow framework, where the flow is no longer

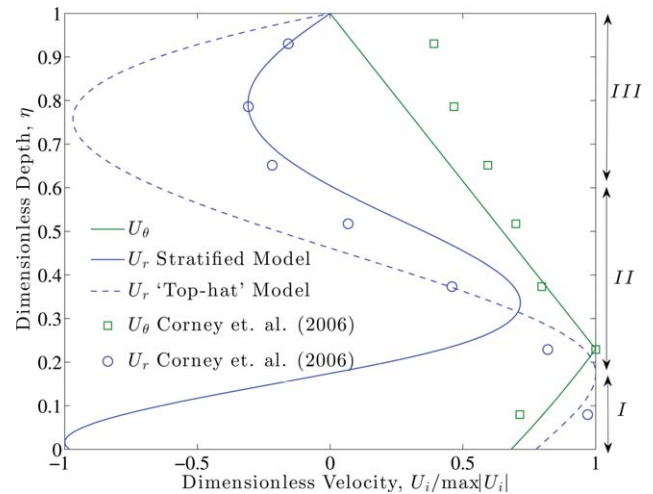


Figure 7. A comparison of the unstratified, top-hat two-dimensional radial flow model (model 1), section 4.1 (denoted with a dashed blue curve), and the stratified two-dimensional radial flow model (model 3), section 4.3 (denoted with a solid blue curve), against the experimental study (Figures 5c and 5d) of *Corney et al.* [2006] (transverse velocity measurements denoted by circles and downstream velocity measurements by squares). Negative radial flow is oriented toward the inner bank and positive radial flow is oriented toward the outer bank. The normalized downstream flow velocity, approximated by the structure function of *Abad et al.* [2011] (20), is denoted by a solid green curve and is always positive. The models are solved subject to zero saline and fluid flux conditions appropriate for a two-dimensional model of a flow within a bounded channel; the Chezy drag coefficient $C_z = 10$. The regions *I*, *II*, and *III* are used to respectively denote areas of near bed, interior, and near interface flow. The regions are defined by the change in the orientation of the flow from inner to outer bank or vice versa.

rotationally invariant, material fluxes can be nonzero. Such radial material transport arises from the inclusion of non-negligible rotational convective transport terms in the mass conservation equations (see (8) and (9) and section 3.2). It is important to note that, whilst convective transport terms may be non-negligible, convective acceleration terms remain negligible in the radial momentum conservation equation (17). In this section, we employ model 4 (Table 1) to describe the vertical structure of radial flow within a three-dimensional flow framework.

[55] If the material fluxes are nonzero, the normalized transverse water slope, \mathcal{S} , and density gradient \mathcal{G} , as defined in (15), comprising the decomposed radial pressure gradient, constrain the radial flow structure (Figure 8). The experimental data of *Abad et al.* [2011] indicate a transverse water slope $\mathcal{S} = \mathcal{O}(1)$, when normalized by δFr_d^2 . However, field data [*Parsons et al.*, 2010] and laboratory experiments [*Keevil et al.*, 2006; *Cossu and Wells*, 2010] indicate that the normalized transverse water slope can be an order of magnitude larger, $\mathcal{S} = \mathcal{O}(10)$. For this reason, we consider normalized transverse water slope variations in the range $-10 \leq \mathcal{S} \leq 10$ (Figure 8), with an equivalent

range also used for the normalized density gradient (i.e., $-10 \leq \mathcal{G} \leq 10$).

[56] We initially consider the radial flow structure in the absence of Coriolis forces (Figures 8e–8h). Negative values of the normalized transverse water slope and positive density gradients indicate components of the radial pressure gradient oriented toward the inner bank, whilst positive water slope and negative density indicate reversed secondary flow toward the outer bank (Figures 3c and 3d). As shown in Figure 8, when the decomposed radial pressure gradient forces balance, secondary flow cells may develop. However, if there is a dominant force acting on the flow (e.g., a large normalized transverse water slope or density gradient), the radial force collapses the rotational secondary flow cell and drives flow toward either the inner or outer bank. In reality, whilst river-normal and river-reversed single-cell secondary flow (Figure 8, *RN* and *RR*) only occupy a limited part of the phase-space, most systems, where radial forces approximately balance, will automatically be within this region. Moreover, as shown in Figure 3, the magnitude of the normalized transverse water slope exceeds that of the normalized transverse density gradient

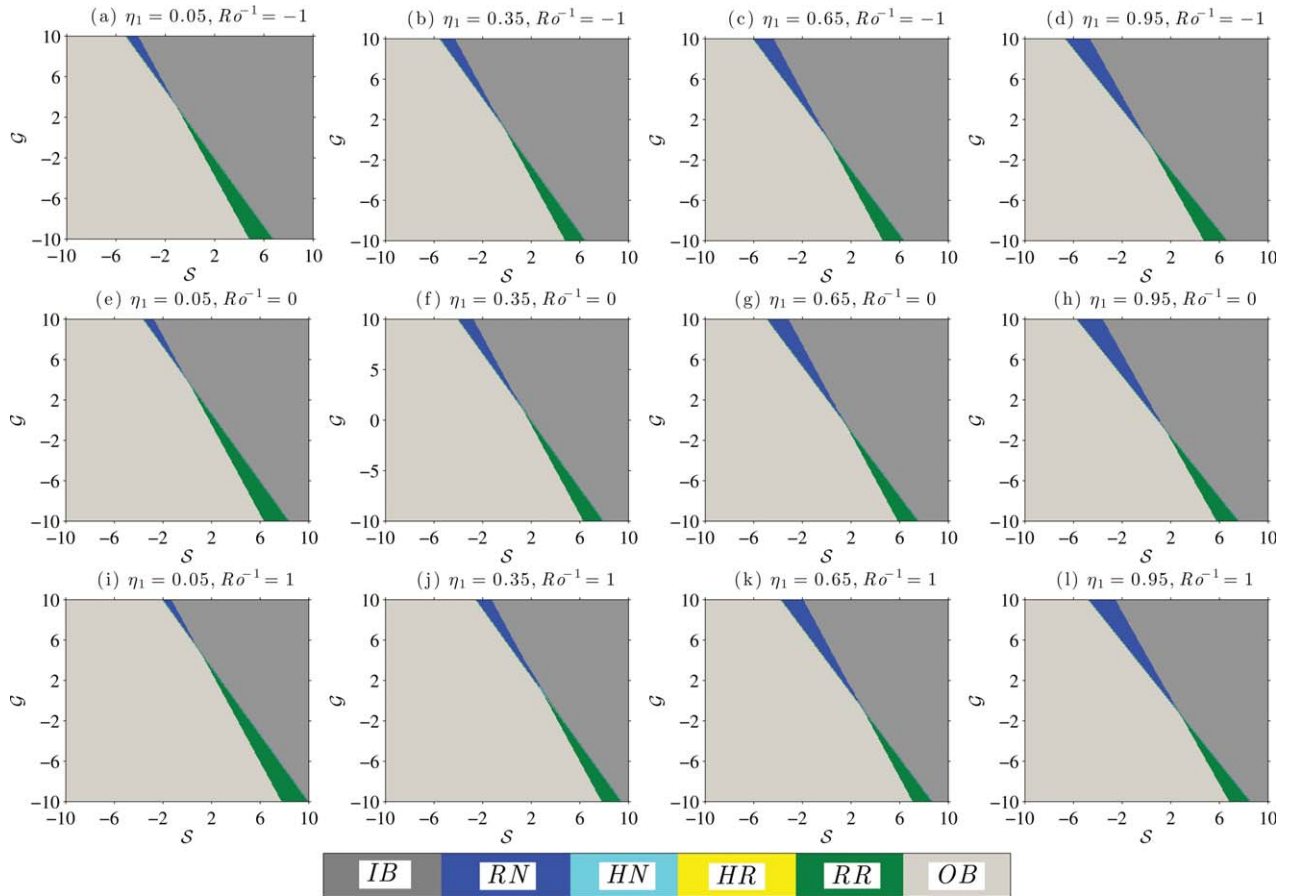


Figure 8. The radial flow structure, model 4, (solid colors) as a function of the normalized (by δFr^2) (15)) water slope, \mathcal{S} , and density gradient, \mathcal{G} . The vertical structure is separated into distinct classes, see Figure 4. Four distinct dimensionless depths of the maximum flow velocity are considered $\eta_1 = 0.05$, 0.35, 0.65, and 0.95. The effects of negative, inner bank-oriented Coriolis forces, $Ro^{-1} = -1$, negligible Coriolis forcing, $Ro^{-1} = 0$, and positive, outer bank-oriented Coriolis forcing, $Ro^{-1} = 1$, are also plotted. The Chezy drag function, specifying the slip velocity (22), $C_z = 15$.

in the near bed layer. Thus, in Figure 8, when neglecting centrifugal and Coriolis forces, river-reversed flow is predominantly found when the decomposed radial pressure gradient forces approximately balance and the normalized transverse water slope $\mathcal{S} > 0$ and normalized transverse density gradient $\mathcal{G} < 0$, whereas river-normal flow is found whilst $\mathcal{S} < 0$ and $\mathcal{G} > 0$.

[57] In Figure 8, variations in the summed force balance result in a transition between river-normal and river-reversed flow, again via the generation of flow composed of multiple helical cells with inner bank-oriented near bed flow. It is noted that, due to the scalings, this transition region is not visible in Figure 8, but it is discussed further below (section 5.1). Further, the dimensionless depth of the downstream flow velocity maximum, η_1 , is shown to affect the phase-space of the radial flow structure, as depicted in Figure 8 for the three different Coriolis forces. With increasing η_1 , the near-bed magnitude of the centrifugal force is decreased. Thus, the proportion of river-normal flow in the phase-space of Figure 8 is increased with increasing η_1 , as discussed in section 4.

[58] Figure 8 also highlights the effect of the Coriolis force on flow dynamics. Constraining the analysis to the region of the phase-space where rotational secondary flow cells develop, we note that, as a result of positive, outer bank oriented, Coriolis forcing altering the force balance equation, there is an increase in the normalized transverse water slope in comparison to the case of negligible Coriolis forcing (Figures 8e–8h, 8i–8l). Conversely, a negative, inner bank oriented, Coriolis forcing results in a comparative decrease in the normalized transverse water slope (Figures 8a–8d, 8e–8h). In a similar fashion, as Coriolis forcing increases, from negative to positive, river-reversed rotational secondary flow becomes more prevalent (Figures 8a, 8e, and 8i). The predicted behavior of the flow-ambient fluid interface agrees with the findings of *Cossu and Wells* [2010, 2013] and *Cossu et al.* [2010] who show that inner bank-oriented Coriolis forcing flattens the water slope (or forces it to increase toward the inner bank), whilst positive Coriolis forces increase the superelevation of the water surface toward the outer bank and enhance river-reversed secondary flow.

[59] By incorporating nonzero radial fluxes into model 4 using a three-dimensional flow framework, the near-bed secondary flow of model 3 discussed in section 4.3 (Figure 6), which was inconsistent with experimental findings, is avoided. Hence, model 4 can be viewed as a generalized form of model 3, with the latter corresponding to the specific case where the material fluxes, dimensionless radial fluid flux Q_{rf} and dimensionless depth-integrated radial density flux Q_{rs} , are negligible (see Table 1).

5.1. Nonnegligible Radial Flux and Resultant Secondary Flow Dynamics

[60] In the three-dimensional flow framework considered here (section 5), convective transport terms (8) and (9), modeling rotational variation of the flow velocity and density, are assumed to be non-negligible. Whilst the net transport of material within the flow must remain zero for a hydrodynamically stable flow, a three-dimensional flow framework

allows variation in the rotational material convection to be balanced by radial material transport (section 3.2).

[61] Two-dimensional models (models 1–3) and three-dimensional models (model 4) of rotational flow are therefore distinguished by the constraints on the dimensionless material fluxes, Q_{rf} and Q_{rs} , where a negative flux implies material transport toward the inner bank and a positive flux implies material transport toward the outer bank. In this section, the magnitude of the radial material fluxes is shown to be the crucial control on the vertical structure of radial flow. Specifically, in Figure 9, the vertical structure of radial flow within a submarine meander is expressed, using model 4, as a function of the magnitude and the sign of the net saline and fluid fluxes. The fluid flux and the depth-integrated radial density flux, necessary to close the radial flow model 4, are only distinct whilst the flow is stratified. Therefore, in Figure 9, we restrict the solutions to $\eta_1 < 0.7$ (see section 2.3 for rationale).

[62] For cases when the material fluxes are negligible, $|Q_{rf}| \ll 1$ and $|Q_{rs}| \ll 1$ (e.g., $< 10^{-3}$ in Figure 9), model 4 reduces to the classical two-dimensional model 3. Variations in either the dimensionless depth of the flow velocity maximum, η_1 , or the magnitude of the Coriolis force, characterized here by the inverse Rossby number (Ro^{-1}), affect the force balance acting on the flow, thereby changing the region of the phase-space in which Q_{rf} and Q_{rs} may be assumed to be negligible (Figures 9a–9i). When $|Q_{rf}| \ll 1$ and $|Q_{rs}| \ll 1$, the predicted near-bed flow velocity does not agree with previous experimental research [*Cossu and Wells*, 2010], suggesting in said study material fluxes were non-negligible.

[63] However, whilst material fluxes are non-negligible, the flow may be river-reversed or river-normal. As the flow is stratified, the near bed contribution of the flow to Q_{rs} will be greater than the near-bed contribution of the flow to Q_{rf} . Therefore, as summarized in Figure 9, if the depth-integrated radial density flux is larger than the fluid flux, $Q_{rs} \gg Q_{rf}$, then the flow is river-reversed. Conversely, if $Q_{rf} \gg Q_{rs}$, then the flow is river-normal. Further, whilst previous theoretical studies have not included non-negligible material fluxes, in section 5.2, we show that they are present in prior experimental studies and are essential to accurate modeling. Moreover, non-negligible material fluxes explain the anomalous experimental data points of secondary flow behavior in the phase space of *Abad et al.* [2011], see Figure 1, who constrained radial fluid flux to be zero.

5.2. Comparison to Experimental Studies of Secondary Flow Within Submarine Meanders

[64] There is insufficient field data to accurately quantify radial and material fluxes in real-world channelized submarine density currents. Instead, we use the experimental results of *Corney et al.* [2006] and the numerical results of *Abad et al.* [2011] to validate our model. From these experiments, we determine the magnitude of the radial fluid flux by integrating over a cubic spline fitted through the experimental results for the radial flow. The stratification model (25) proposed by *Abad et al.* [2011] is used to determine the dimensionless depth-integrated radial density flux. In terms of the maximum flow velocity, the material fluxes, see equations (37) and (38), are thus determined as:

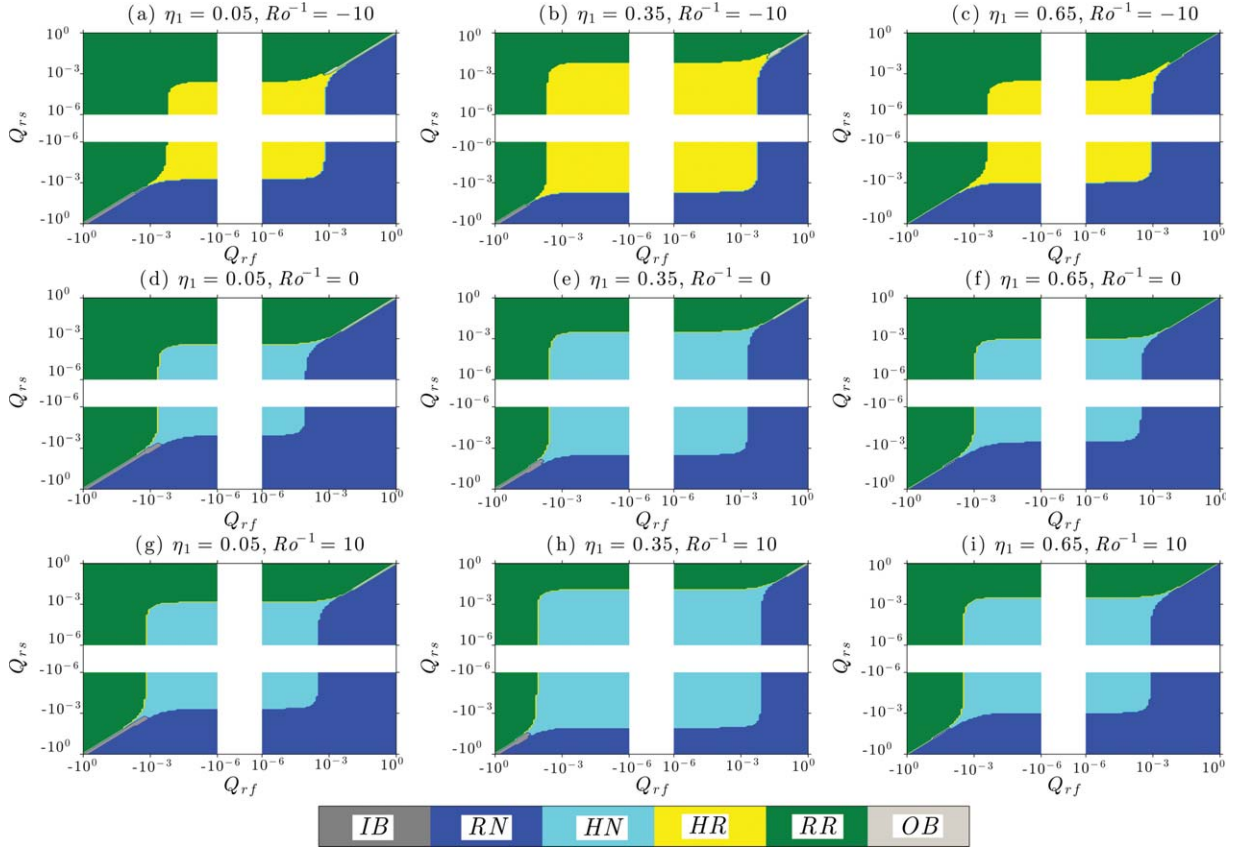


Figure 9. The radial flow structure, model 4, (solid colors) as a function of the depth-integrated fluid flux, Q_{rf} , and the depth-integrated radial density flux, Q_{rs} . The vertical structure is separated into distinct classes, see Figure 4. Three distinct dimensionless depths of the maximum flow velocity are considered $\eta_1 = 0.05, 0.35$, and 0.65 , such that the flow is stratified and the flux conditions (37) and (38) are distinct and constrain radial flow solutions. The effect of inner bank-oriented ($Ro^{-1} = -10$), negligible ($Ro^{-1} = 0$), and outer bank-oriented ($Ro^{-1} = 10$) Coriolis forcing is shown. The Chezy drag function, specifying the slip velocity (22), $C_z = 15$.

$$\frac{Q_{rfC}}{\max |U_{rC}|} = \frac{\int_0^\infty U_r d\eta}{\max |U_{rC}|} = 0.2503 \quad \text{and} \quad (40)$$

$$\frac{Q_{rsC}}{\max |U_{rC}|} = \frac{\int_0^\infty U_r \varphi d\eta}{\max |U_{rC}|} = 0.5078,$$

where the subscript C is used to denote the measured flux and velocity. Both the saline and fluid fluxes in equation (40) are seen to be positive and non-negligible in comparison to the magnitude of the radial fluid velocity. The experimental results of *Abad et al.* [2011] (experiment 3b, Figure 23), denoted by subscript A , may also be integrated to find non-negligible fluid flux and the depth-integrated radial density flux, where $Q_{rfA}/\max |U_{rA}| = Q_{rsA}/\max |U_{rA}| = 0.0994$ using (25). This analysis of the radial fluid flux and the depth-integrated radial density flux in itself highlights that a three-dimensional model is likely to be needed to adequately describe the secondary flow behavior within stratified submarine flows.

[65] To model the experimental results of *Corney et al.* [2006], where the flow is stratified (25), it is assumed that

the ratio of the saline to fluid flux of the experiments is equivalent to that of the three-dimensional radial flow model, i.e.:

$$\frac{Q_{rsC}}{Q_{rfC}} = \frac{Q_{rs}}{Q_{rf}}. \quad (41)$$

[66] The three-dimensional model for radial fluid flow can now be fitted to the experimental results using the depth-integrated radial fluid flux, Q_{rf} , as an unknown parameter. From (41), and by minimizing the sum relative error, E_r , between the experimental results and numerical model throughout the flow depth,

$$E_r = \int_0^1 \frac{|U_{rfC} - U_{rf}|}{|U_{rC}|}, \quad (42)$$

the depth-integrated fluid flux and the depth-integrated radial density flux are determined to be

$$Q_{rf} = 0.0160 \quad \text{and} \quad Q_{rs} = 0.0324 \quad (43)$$

[67] In Figure 10a, the three-dimensional model results are compared to the *Corney et al.* [2006] data. In comparison

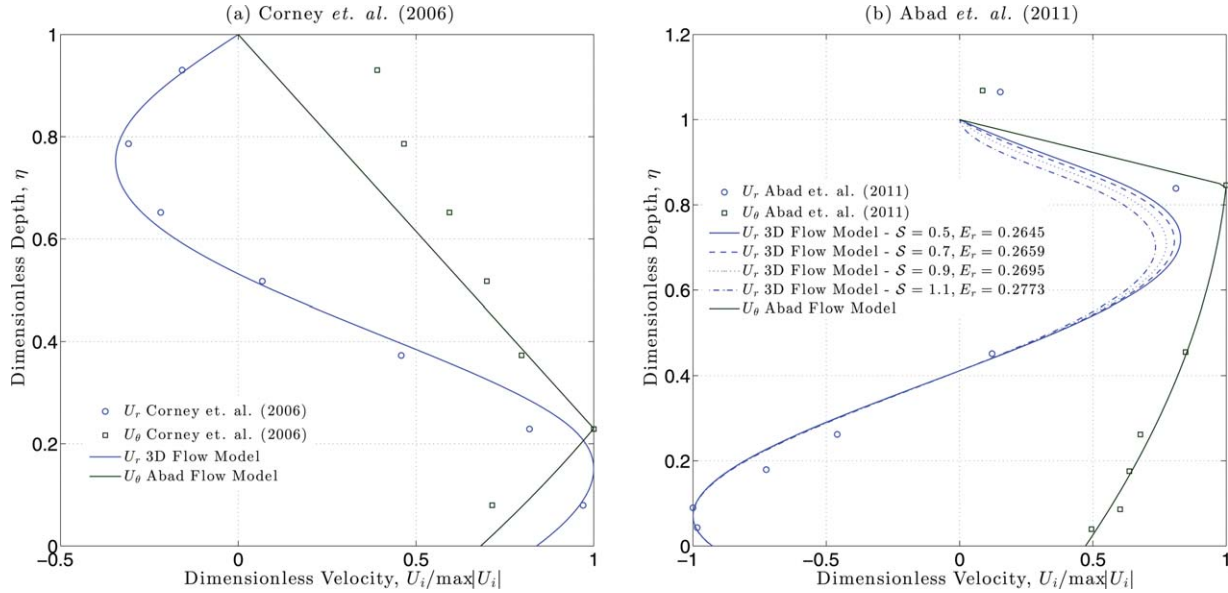


Figure 10. Radial component of flow, derived from model 4, within a submarine meander, as a function of flow depth (denoted by blue curves). Theoretical results of model 4 are compared to the experimental results of primary and secondary flow published by (a) *Corney et al.* [2006] and (b) *Abad et al.* [2011]. Experimental measurements of transverse velocity are denoted by circles and downstream velocity measurements by squares. Negative radial flow is oriented toward the inner bank and positive radial flow is oriented toward the outer bank. In Figures 10a and Figures 10b, the normalized downstream flow velocity, approximated by the structure function of *Abad et al.* [2011] (20), is denoted by a solid green curve and is always positive. In the theoretical-experimental comparisons, the Chezy drag function, $C_z = 10$, and Coriolis force is assumed to be negligible, $Ro^{-1} = 0$. In Figure 10a, the depth-integrated radial density flux was determined as a function of the fluid flux, based on the stratification model of *Abad et al.* [2011] (25). In Figure 10b, the three-dimensional flow model was fitted to the experimental results as a function of the normalized water slope, \mathcal{S} , and density gradient, \mathcal{G} .

to the two-dimensional model discussed in the previous section (Figure 7), the three-dimensional model shows a much closer qualitative and quantitative agreement to the experimental observations. For the three-dimensional model, the sum relative error $E_r = 0.2084$, whereas for the unstratified and stratified two-dimensional models $E_r = 2.2727$ and $E_r = 1.4770$, respectively.

[68] Based on the dimensionless depth of maximum flow velocity (Figure 10b), the experimental submarine flow recorded by *Abad et al.* [2011] is assumed to be unstratified (25). Thus, flow solutions are obtained by minimizing the relative error (42) as a function of the normalized transverse water slope, \mathcal{S} , and normalized transverse density gradient, \mathcal{G} .

[69] In Figure 10b, the radial flow model is shown to compare well to data from experiment 3b of *Abad et al.* [2011]. In experiment 3b, the normalized transverse water slope is $\mathcal{S} = 1.08$, as derived from *Abad et al.* [2011]. In Figure 10b, the secondary flow structure is plotted for a range of \mathcal{S} , where the sum relative error (42) is minimized as a function of the normalized transverse density gradient, \mathcal{G} . As shown in Figure 10b, with \mathcal{S} decreasing from 1.1, the sum relative error between the theory and experimental results is seen to decrease. The discrepancy between the optimal value of \mathcal{S} in the theoretical model and the measured value of \mathcal{S} in the experiment may be explained by the difference in the definition of the flow-ambient fluid interface used in the theoretical model (29) and that used by

Abad et al. [2011] (30). Indeed, it is noted that by rescaling the dimensionless depth of the flow to $\eta = 1.1$, such that the experimental measurements of flow velocity tend to zero at the flow interface [*Abad et al.*, 2011], the accuracy of the theoretical model is improved. Moreover, the meandering channel used in the experimental setup of *Abad et al.* [2011] is highly nonuniform, with no definitive path along which the radius of curvature is constant. Naturally, the discrepancy between the experimental and theoretical results may in part also be attributed to experimental error or simply due to the simplified nature of the theoretical model used herein.

6. Discussion

6.1. Flow Dynamics

[70] In submarine density currents flow, superelevation is enhanced as the flow banks around a meander bend due to the reduced density difference between the flow and ambient fluid [*Pirmez and Imran*, 2003]. Approaching the apex of a meander bend flow superelevation increases, and the velocity core moves toward the outer bank or vice-versa whilst moving away from the apex [*Imran et al.*, 1999]. Such variation in superelevation and velocity of the flow along a curve of constant radius can only be explained by net radial transport of material. As has been discussed in section 3.2, the net radial transport of material balances the variation in the rotational material transport terms of the

mass conservation equation, see (37) and (38). Furthermore, in submarine meander bends topographic and dynamic forces, including any variation from a uniform channel bathymetry of constant radius, the formation of point-bars and scours, flow overspill and Coriolis forces, may act to enhance the magnitude of radial material fluxes (see sections 1 and 3.2). Moreover, further research, detailing how radial material fluxes depend on bulk flow conditions and changes in channel topography would enable the model to make generic predictions of secondary flow in highly complex real-world systems such as individual channel bends in the Amazon, Zaire, or Mississippi submarine fans without resorting to numerically intensive flow field solutions.

[71] For flow in a straight channel, with vanishing Coriolis forces, there is no superelevation of the flow [Cossu *et al.*, 2010]; thus, it may be assumed that cross-sectional channel relief is approximately symmetrical. However, within a meander bend, superelevation of the flow results in asymmetric cross-sectional channel relief. Indeed, Pirmez and Imran [2003] noted that there is consistent cross-sectional asymmetry, with deepest flow toward the outer bank, throughout the entire Amazon submarine canyon-fan system. Thus, the magnitude of cross-sectional channel

asymmetry at the meander apex is indicative of the magnitude of radial material fluxes, and therefore, the orientation of near bed flow, see section 5.1.

[72] Stratification of submarine flows enhances near bed density flux and diminishes near flow interface density flux (Figure 11). As a result of flow stratification, the depth-integrated radial density flux is greater than the magnitude of the fluid flux, whilst the transverse velocity maximum is near the flow bed. Indeed, this conclusion may also be drawn from prior three-dimensional numerical [see, e.g., Kassem and Imran, 2004; Giorgio Serchi *et al.*, 2011] and experimental studies [see, e.g., equations (40) and (43) of this paper and Corney *et al.*, 2006; Abad *et al.*, 2011] of submarine meanders, as well as field studies of stratified estuarine meanders where advective contributions to the secondary flow momentum balance equations (17) are well recognized [see, e.g., Chant and Wilson, 1997]. From the results of section 5.1, it is therefore concluded that, whilst material fluxes are non-negligible and oriented toward the outer bank, the near-bed orientation of secondary flow in stratified submarine meanders is predominantly river-reversed, but predominantly river-normal when the material fluxes are negligible or oriented toward the inner bank (Figure 9). This suggests that, in the initial section of a

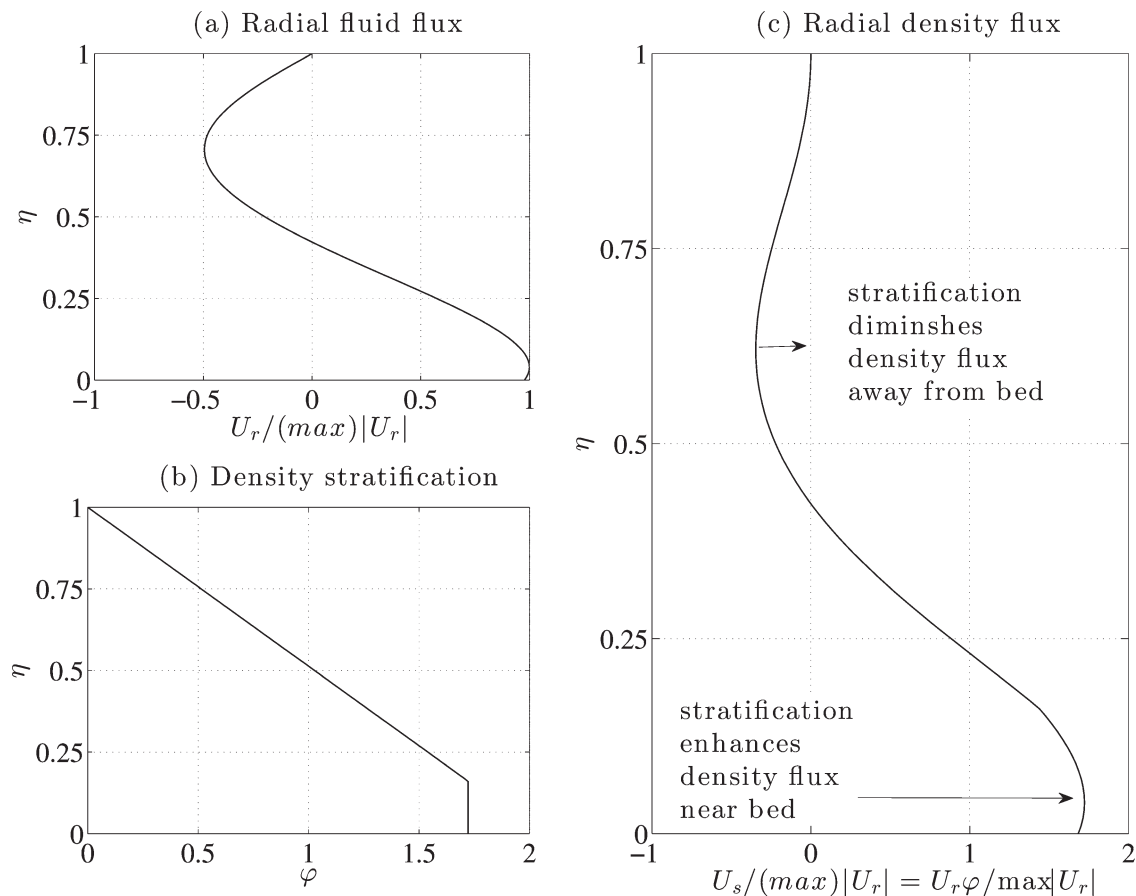


Figure 11. The radial density flux is given by the product of the (a) radial fluid flux and (b) radial density flux. (c) Stratification of the flow enhances the near bed radial density flux but diminishes it away from the bed. Here the depth-integrated radial density flux, Q_{rs} , is four times larger than the corresponding radial fluid flux, Q_{rf} .

meander bend, net outer bank material flux drives a single helical cell with river-reversed flow, this initial period of flow behavior will extend beyond the meander apex, as flow lags behind topographic forcing [Parker *et al.*, 1983; Imran *et al.*, 1999]. After the bend apex, waning net material fluxes may create a second helical cell, forming a helical couplet [Imran *et al.*, 2007], with inner bank-oriented near bed secondary flow (see Figure 9). Past the bend apex, as the magnitude of the material flux directed toward the inner bank is likely increased, the upper cell of the helical couplet is destroyed, and the flow consists of single helical cell that is river-normal.

[73] Prior research [Pirmez and Imran, 2003] has shown that flow dynamics systematically vary throughout submarine canyon-fan systems. In the proximal region of submarine canyon-fan systems, the flow is frequently supercritical, often incising deep canyons into the bedrock [e.g., Khripounoff *et al.*, 2003], see zones I and II of Figure 12. Within these proximal regions, the supercritical flow has a downstream velocity maximum near the flow bed, implying that the near-bed secondary flow is dominated by outer bank-oriented centrifugal forces [Abad *et al.*, 2011]. Bounded within the channel, superelevation of the flow in submarine meander bends will be large due to the reduced density difference between the flow and ambient fluid. Indeed, whilst typical transverse water slopes at the apex of subaerial meander bends, where the ratio of flow to atmospheric density is of the order 800 ($\text{kgm}^{-3}/\text{kgm}^{-3}$), are of

the order 10^{-4} (m/m) in magnitude [Leopold, 1982], the transverse water slope for submarine density currents, where the ratio of flow to ambient fluid density may be as small as 1.01, are of the order 10^{-2} [Komar, 1969; Pirmez and Imran, 2003]. Figure 8 shows that secondary flow is more likely to be orientated toward the outer bank with increasing normalized water slope gradient (15). Thus, the larger transverse water slope of submarine flows, when compared to subaerial flows, suggests that outer bank-orientated flow should predominate. Moreover, it follows that greater radial material fluxes are needed to generate larger transverse water slopes and therefore that river-reversed secondary flow is likely at the apices of submarine meander bends where superelevation of the flow is greatest.

[74] In the lower fan, the flow slows and deepens, see zones II and III of Figure 12. No longer constrained within deep canyons and valleys, the flow is bounded by shallow, self-formed, levees [Imran *et al.*, 2002; Yu *et al.*, 2006; Nakajima *et al.*, 2009], often 2 to 5 m in elevation [Pirmez and Imran, 2003]. As the flow becomes subcritical, the flow velocity maximum moves away from the flow bed. One might expect that at the bend apex the flow becomes river-normal, as per the analysis of Abad *et al.* [2011] (Figure 1). However, in such shallow channels, superelevation would result in significant flow overspill from the channel [Piper and Normark, 1983; Savoye *et al.*, 2009], resulting in non-negligible radial material transport, discussed in section 5. Material loss, predominant on the outer bank of the

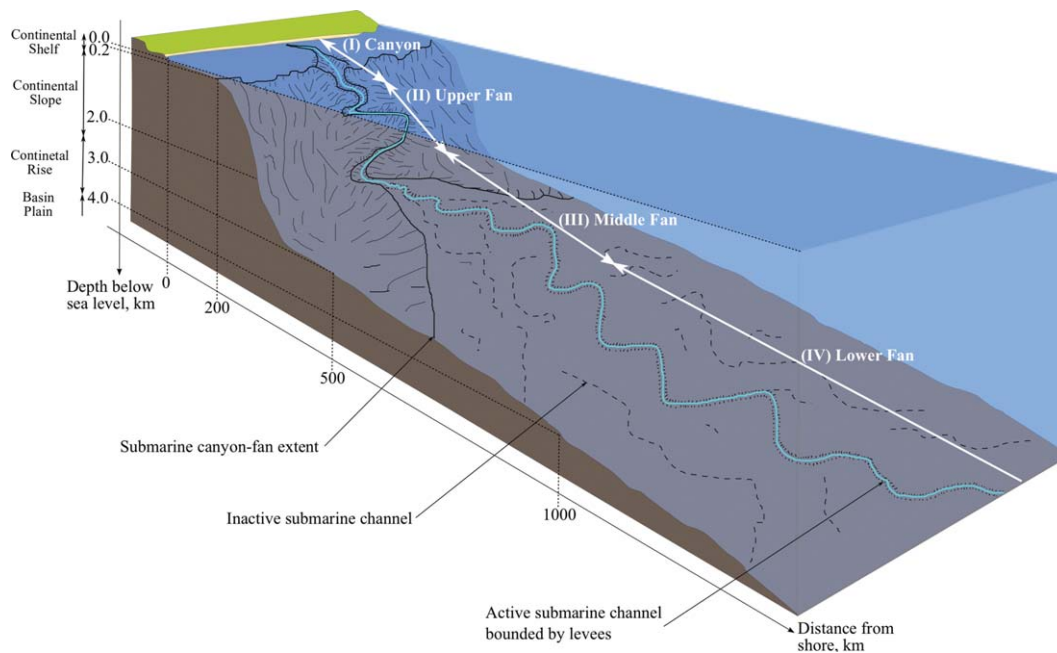


Figure 12. Schematic view of submarine canyon-fan system, with key flow regions. High energy, particulate-laden density currents within submarine canyons, entrain ambient fluid, and may also entrain sediment (I). Given non-negligible radial fluxes, driven by convective effects, flow stratification implies that secondary flow structure is river-reversed. Flow slows causing deposition of sediment from suspension, (II)–(III), and the velocity maximum is raised away from the bed. Here non-negligible outer bank-oriented material fluxes, with associated river-reversed circulation, may be driven by overspill from shallow bounding levees. Moreover, in large-scale meander bends, where Coriolis force is non-negligible, the additional forcing can cause transition in the orientation of near bed flow or enhance or diminish the elevation of the flow-ambient fluid interface.

channel and resultant of flow overspill, would have the effect of enhancing the radial material fluxes, forcing river-reversed secondary flow. Indeed, the very presence of such bounding levees indicates that there is significant overspill and material loss from such channel systems [Peakall *et al.*, 2000]. Flow dynamics in the distal reaches of submarine canyon-fan systems, zone *IV* of Figure 12, are less well understood. Here the flow slows and may be significantly deeper than the mean channel relief [Pirmez and Imran, 2003; Savoye *et al.*, 2009], allowing the majority of the flow to effectively bypass topographic, and resultant flow dynamic, forcing.

[75] Throughout the submarine canyon-fan system (Figure 12), the Coriolis force is a secondary control on the near-bed orientation of radial fluid flow [see sections 4 and 5 and Komar, 1969; Cossu and Wells, 2010, 2013; Cossu *et al.*, 2010]. If the material fluxes are negligible, positive (outer bank-oriented) and negative (inner bank-oriented) Coriolis forcing (Figure 2) may cause transitions to river-normal or river-reversed near bed flow, respectively (Figure 9). Moreover, Coriolis forces will enhance inner or outer bank superelevation of the flow-ambient fluid interface (Figure 8), promoting channel flow overspill, enhancing the magnitude of the radial material flux, thereby driving river-normal or river-reversed secondary flow.

6.2. Impacts for Sedimentation

[76] The three-dimensional flow field, discussed above, plays a key role in controlling the nature and location of sediment deposition within sinuous channels. At a first-order level, the nature of sedimentation in submarine channels is a function of whether flows are dominantly bypassing with traction-dominated deposition at their base or whether there is large-scale deposition from suspension as flows collapse [Kane *et al.*, 2008; Amos *et al.*, 2010]. In the latter case, the orientation of the secondary basal flow will have a limited effect since the sediment undergoes little if any tractional movement. Instead sedimentation is concentrated on the outside of submarine bends where flow interacts with the outer bank, producing outer bank bars [Nakajima *et al.*, 2009; Huang *et al.*, 2012; Ezz *et al.*, 2013; Janocko *et al.*, 2013].

[77] For traction-dominated deposition, the three-dimensional flow field is important. Consideration of a two-dimensional flow field at bend apices would suggest that river-like secondary flow with inward-directed basal flow produces inner-bend deposition equivalent to the point-bars of rivers, with a deep pool at the outer bank [Abad *et al.*, 2011]. In contrast, reversed secondary flow with outward-directed basal flow could be expected to produce a pool toward the inner bank and shallower outer bank sedimentation, termed “antipoint-bar morphology” by Abad *et al.* [2011]. However, if we consider the full three-dimensional nature of the flow field, then particles are not solely restricted to move transverse to the bend (as in the two-dimensional case above); in fact, particles will move dominantly downstream with only a relatively small cross-stream component [Nelson and Smith, 1989; Bridge, 1992]. Furthermore, deposition occurs primarily where there is a convergence of sediment flux [Nelson and Smith, 1989]. For river-like secondary flow, this will result in a point-bar similar to a river centered around the bend apex

[Janocko *et al.*, 2013], where flow is inwardly directed producing a sediment flux convergence. However, for reversed secondary flow, the point at which flow becomes inwardly directed, and at which sediment flux converges, is moved further downstream past the bend apex [Keevil *et al.*, 2006; Peakall *et al.*, 2007; Amos *et al.*, 2010]. This in turn results in point-bars that are positioned further around, or downstream of, the bend apex, as has been shown both experimentally [Peakall *et al.*, 2007; Amos *et al.*, 2010] and theoretically [Darby and Peakall, 2012] for submarine channels. At the bend apex itself, gradients tend to be relatively low [Peakall *et al.*, 2007; Darby and Peakall, 2012] but do not result in the “antipoint-bar” morphology postulated by Abad *et al.* [2011] when considering the two-dimensional case. In fact, the overall transverse gradients of the point bar for reversed secondary flow are an order or a magnitude lower than their fluvial counterparts Darby and Peakall [2012].

[78] We note that the three-dimensional fluid flow in submarine bends can be further complicated by a wide range of other processes, these in turn influencing sedimentation patterns. Notable factors include: (i) the interaction of overbank flow with in-channel flow, particularly where overbank flow re-enters the channel [Amos *et al.*, 2010; Janocko *et al.*, 2013]; (ii) the presence of flow separation at sharp bends leading to sedimentation in these zones [Straub *et al.*, 2008, 2011]; and (iii) run-up and collapse of material at steep-sided banks in submarine channel simulations [Straub *et al.*, 2008, 2011; Janocko *et al.*, 2013]. Combinations of these can lead to deposition occurring at a wide range of positions around a bend [see Janocko *et al.*, 2013]. In the absence of such additional factors, the present study suggests that, for much of their longitudinal extent, sinuous submarine channels will show point-bar deposits that are preferentially located downstream of bend apices and are relatively thin in comparison to their fluvial counterparts.

7. Conclusions

[79] Analytical solutions have been constructed to investigate the rotational behavior of secondary flow within submarine channels. For the first time, this research has unified and systematically explored the fundamental physical processes controlling secondary flow structure within submarine meander systems, elucidating: (i) the reasons for the formation of multiple helical cells, (ii) the importance of Coriolis forcing, and; (iii) the significance of both radial and vertical density stratification effects.

[80] The radial flow models presented herein have been discussed in terms of the balance of centrifugal, Coriolis, and radial pressure gradient forces driving radial variations in turbulent shear stress, the latter being described in terms of the transverse velocity. Here we demonstrate that the radial flow structure in submarine meander bends is strongly dependent on flow baroclinicity and the resultant magnitudes of radial material fluxes. This range of key parameters means that previous phase-space diagrams, see Figure 1, are not sufficient to capture the fundamental physical processes driving secondary flow within submarine channel bends. Moreover, the key role of the radial material fluxes as highlighted in our work also corrects the discrepancy

between previous theoretical predictions and experimental observations of secondary flow circulation in submarine meanders. Furthermore, this research has shown that, when radial material fluxes are negligible, the addition of Coriolis forces can cause a transition between river-reversed and river-normal secondary flow or vice versa. Coriolis driven transitions in secondary flow dynamics are consistent with the hypothesis that near-bed submarine flow orientation, and thus submarine meander system sinuosity, is in part controlled by latitude [Peakall et al., 2012; Cossu and Wells, 2013]. Moreover, it has been demonstrated that, when radial material fluxes are non-negligible, Coriolis forces act to enhance (positive Coriolis) or diminish (negative Coriolis) the elevation of the flow-ambient fluid interface, as is consistent with prior experimental studies.

[81] Analysis of both two- and three-dimensional flow closures for the boundary conditions on the radial component of secondary flow demonstrates that submarine channels have to be treated as a three-dimensional problem, since they exhibit large radial material fluxes. These fluxes are driven by the large-scale (orders of magnitude higher than river channels) superelevation exhibited in submarine channel bends. The propensity of such flows to overspill, particularly at channel bends (as demonstrated by the frequent presence of levees), also results in substantial net fluxes, directed toward the outer banks, in the regions up to and beyond bend apices. Previous research has highlighted roughness and the position of the downstream velocity maximum as controls of the near-bed orientation of secondary flow. However, here we demonstrate that it is the magnitude of radial material fluxes, arising from superelevation and overspill, that is the key control on the secondary flow regime.

[82] Prior studies of secondary circulation in submarine channels, which neglect three-dimensional flow and baroclinic effects, have underestimated the propensity for river-reversed flow in submarine canyon-fan systems. Previous work has suggested that secondary flow reversal is likely to be common mostly within the proximal regions of submarine canyons and is unlikely in the more distal regions of submarine fans. However, we have shown that river-reversed flows are likely to be induced where flow overspill generates strong, outer bank-oriented, radial fluxes as is likely the case even in the distal parts of submarine canyon-fan systems. Given that the direction of the near bed radial flow is known to have a strong influence on sediment transport processes within meander bends, our conclusion—that the propensity of river-reversed submarine meander flow has likely been significantly underestimated—has significant implications in the context of seeking to understand facies patterns and bend topography within submarine channel systems.

Notation

α	latitude.
β	salinity conversion coefficient.
δ	flow aspect ratio.
η_0	roughness height.
η_1	depth of flow velocity maximum.

η_2	depth of unstratified flow.
θ	rotational angle.
ν_t	Eddy viscosity.
ρ_f, ρ_a	fluid, ambient fluid density.
φ	normalized density shape function.
ϕ	excess density.
$\bar{\phi}$	average excess density.
χ	slip parameter.
E_r	sum relative error.
Fr_d	densimetric Froude number.
f_1, f_2	pressure structure functions.
f_s	density shape function.
h	flow depth.
g	specific gravity.
\mathcal{G}	normalized density gradient.
L	radius of curvature.
P	gauge pressure.
q_{rf}, Q_{rf}	radial fluid flux.
q_{rs}, Q_{rs}	radial density flux.
r	radial distance across channel.
s_a, s_b	ambient fluid, flow salinity.
Re	Reynolds number.
Ro	Rossby number.
\mathcal{S}	normalized water slope.
T_p	downstream velocity shape function.
\bar{u}_θ	average downstream flow velocity.
u_r, U_r	transverse flow velocity.
u_θ, U_θ	downstream flow velocity.
z, η	depth from flow bed.

[83] **Acknowledgments.** This research was supported by awards (NE/F020120/1 and NE/F020511/1) from the Natural Environmental Research Council (NERC).

References

- Abad, J. D., O. E. Sequeiros, B. Spinewine, C. Pirmez, M. H. Garcia, and G. Parker (2011), Secondary current of saline underflow in a highly meandering channel: experiments and theory, *J. Sediment. Res.*, *81*, 787–813.
- Amos, K. J., J. Peakall, P. W. Bradbury, M. Roberts, G. Keevil, and S. Gupta (2010), The influence of bend amplitude and planform morphology on flow and sedimentation in submarine channels, *Mar. Pet. Geol.*, *27*(7), 1431–1447.
- Best, J. L., R. A. Kostaschuk, J. Peakall, P. V. Villard, and M. Franklin (2005), Whole flow field dynamics and velocity pulsing within natural sediment-laden underflows, *Geology*, *33*(10), 765–768.
- Bridge, J. S. (1992), A revised model for water-flow, sediment transport, bed topography and grain-size sorting in natural river bends, *Sedimentology*, *40*(4), 801–810.
- Bridge, J. S. (1993), Description and interpretation of fluvial deposits: A critical perspective, *Water Resour. Res.*, *28*, 999–1013.
- Chant, R. J., and R. E. Wilson (1997), Secondary circulation in a highly stratified estuary, *J. Geophys. Res.*, *102*, 23–23.
- Chernetsky, A. S., H. M. Schuttelaars, and S. A. Talke (2010), The effect of tidal asymmetry and temporal settling lag on sediment trapping in tidal estuaries, *Ocean Dyn.*, *60*(5), 1219–1241.
- Chough, S. K., and R. Hesse (1980), The Northwest Atlantic Mid-Ocean Channel of the Labrador Sea; III, Head spill vs. body spill deposits from turbidity currents on natural levees, *J. Sediment. Res.*, *50*(1), 227–234.
- Corney, R. K. T., J. Peakall, D. R. Parsons, L. Elliott, K. J. Amos, J. L. Best, G. Keevil, and D. B. Ingham (2006), The orientation of helical flow in curved channels, *Sedimentology*, *53*(2), 249–257.
- Corney, R. K. T., J. Peakall, D. R. Parsons, L. Elliott, J. L. Best, R. E. Thomas, G. Keevil, D. B. Ingham, and K. J. Amos (2008), Reply to Discussion of Imran et al. on “The orientation of helical flow in curved channels” by Corney et al., *Sedimentology*, *53*, 249–257, *Sedimentology*, *55*(1), 241–247.

- Cossu, R., and M. G. Wells (2010), Coriolis forces influence the secondary circulation of gravity currents flowing in large-scale sinuous submarine channel systems, *Geophys. Res. Lett.*, *37*, L17603, doi:10.1029/2010GL044296.
- Cossu, R., and M. G. Wells (2013), The evolution of submarine channels under the influence of Coriolis forces: Experimental observations of flow structures, *Terra Nova*, *25*, 67–71.
- Cossu, R., M. G. Wells, and A. Wählin (2010), Influence of the Coriolis force on the velocity structure of gravity currents in straight submarine channel systems, *J. Geophys. Res.*, *115*, C11016, doi:10.1029/2010GL044296.
- Curry, J. R., F. J. Emmel, and D. G. Moore (2002), The Bengal Fan: Morphology, geometry, stratigraphy, history and processes, *Mar. Pet. Geol.*, *19*(10), 1191–1223.
- Darby, S. E., and J. Peakall (2012), Modelling the equilibrium bed topography of submarine meanders that exhibit reversed secondary flows, *Geomorphology*, *164*, 99–109.
- Das, H. S., J. Imran, C. Pirmez, and D. Mohrig (2004), Numerical modeling of flow and bed evolution in meandering submarine channels, *J. Geophys. Res.*, *109*, C10009, doi:10.1029/2002JC001518.
- Davies, P. A., A. K. Wählin, and Y. Guo (2006), Laboratory and analytical model studies of the Faroe Bank Channel deep-water outflow, *J. Phys. Oceanogr.*, *36*(7), 1348–1364.
- Dietrich, W. E., and P. Whiting (1989), Boundary shear stress and sediment transport in river meanders of sand and gravel, in *River Meandering*, AGU Water Resour. Monogr., vol. 12, edited by S. Ikeda and G. Parker, pp. 1–50, Washington D. C.
- Dorrell, R. M., and A. J. Hogg (2012), Length and time scales of response of sediment suspensions to changing flow conditions, *J. Hydraul. Eng.*, *138*(5), 430–439.
- Dyer, K. R. (1973), *Estuaries: A Physical Introduction*, John Wiley, London.
- Dyer, K. R. (1989), Estuarine flow interaction with topography—Lateral and longitudinal effects, in *Estuarine Circulation*, vol. 7, edited by B. Neilson, A. Kuo, and J. Brubake, pp. 39–59, Humana Press, N. J.
- Engelund, F. (1974), Flow and bed topography in channel bends, *J. Hydraul. Div. Am. Soc. Civil Eng.*, *100*(11), 1631–1648.
- Ezz, H., A. Cantelli, and J. Imran (2013), Experimental modeling of depositional turbidity currents in a sinuous submarine channel, *Sediment. Geol.*, *290*, 175–187.
- Fischer, H. B. (1976), Mixing and dispersion in estuaries, *Ann. Rev. Fluid Mech.*, *8*(1), 107–133.
- Giorgio Serchi, F. G., J. Peakall, D. B. Ingham, and A. D. Burns (2011), A unifying computational fluid dynamics investigation on the river-like to river-reversed secondary circulation in submarine channel bends, *J. Geophys. Res.*, *116*, C06012, doi:10.1029/2010JC006361.
- Herbert, A. W., C. P. Jackson, and D. A. Lever (1988), Coupled ground-water flow and solute transport with fluid density strongly dependent upon concentration, *Water Resour. Res.*, *24*(10), 1781–1795.
- Huang, H., J. Imran, and C. Pirmez (2012), The depositional characteristics of turbidity currents in submarine sinuous channels, *Mar. Geol.*, *329*–*331*, 93–102.
- Imran, J., G. Parker, and C. Pirmez (1999), A nonlinear model of flow in meandering submarine and subaerial channels, *J. Fluid Mech.*, *400*(1), 295–331.
- Imran, J., G. Parker, and P. Harff (2002), Experiments on incipient channelization of submarine fans, *J. Hydraul. Res.*, *40*(1), 21–32.
- Imran, J., A. Kassem, and S. M. Khan (2004), Three-dimensional modeling of density current. I. Flow in straight confined and unconfined channels, *J. Hydraul. Res.*, *42*(6), 578–590.
- Imran, J., M. Islam, H. Huang, A. Kassem, J. Dickerson, C. Pirmez, and G. Parker (2007), Helical flow couplets in submarine gravity underflows, *Geology*, *35*(7), 659–662.
- Imran, J., M. A. Islam, and A. Kassem (2008), “The orientation of helical flow in curved channels” by Corney et al., *Sedimentology*, Vol. 53, pp. 249–257—discussion, *Sedimentology*, *55*(1), 235–239.
- Islam, M. A., and J. Imran (2008), Experimental modeling of gravity underflow in a sinuous submerged channel, *J. Geophys. Res.*, *113*, C07041, doi:10.1029/2007JC004292.
- Janocko, M., M. B. J. Cartigny, W. Nemeč, and E. W. M. Hansen (2013), Turbidity current hydraulics and sediment deposition in erodible sinuous channels: Laboratory experiments and numerical simulations, *Mar. Pet. Geol.*, *41*, 222–249.
- Kane, I. A., W. D. McCaffrey, and J. Peakall (2008), Controls on sinuosity evolution within submarine channels, *Geology*, *36*(4), 287–290.
- Kassem, A., and J. Imran (2004), Three-dimensional modeling of density current. II. Flow in sinuous confined and unconfined channels, *J. Hydraul. Res.*, *42*(6), 591–602.
- Keevil, G., J. Peakall, J. L. Best, and K. J. Amos (2006), Flow structure in sinuous submarine channels: Velocity and turbulence structure of an experimental submarine channel, *Mar. Geol.*, *229*(3), 241–257.
- Keevil, G., J. Peakall, and J. L. Best (2007), The influence of scale, slope and channel geometry on the flow dynamics of submarine channels, *Mar. Pet. Geol.*, *24*(6–9), 487–503.
- Khripounoff, A., A. Vangriesheim, N. Babonneau, P. Crassous, B. Dennielou, and B. Savoye (2003), Direct observation of intense turbidity current activity in the Zaire submarine valley at 4000 m water depth, *Mar. Geol.*, *194*(3–4), 151–158.
- Klaucke, I., R. Hesse, and W. B. F. Ryan (1997), Flow parameters of turbidity currents in a low-sinuosity giant deep-sea channel, *Sedimentology*, *44*(6), 1093–1102.
- Klaucke, I., R. Hesse, and W. B. F. Ryan (1998), Morphology and structure of a distal submarine trunk channel: The Northwest Atlantic Mid-Ocean Channel between lat 53° N and 44° 30′ N, *Geol. Soc. Am. Bull.*, *110*(1), 22–34.
- Kolla, V., H. W. Posamentier, and L. J. Wood (2007), Deep-water and fluvial sinuous channels—Characteristics, similarities and dissimilarities, and modes of formation, *Mar. Pet. Geol.*, *24*, 388–405.
- Komar, P. D. (1969), The channelized flow of turbidity currents with application to Monterey deep-sea fan channel, *J. Geophys. Res.*, *74*(18), 4544–4558.
- Komar, P. D. (1970), The competence of turbidity current flow, *Geol. Soc. Am. Bull.*, *81*(5), 1555–1562.
- Lacy, J. R., and S. G. Monismith (2001), Secondary currents in a curved, stratified, estuarine channel, *J. Geophys. Res.*, *106*, 283–302.
- Leopold, L. B. (1982), Water surface topography in river channels and implications for meander development, in *Gravel-Bed Rivers*, pp. 359–383, John Wiley, New York.
- Lesshaft, L., E. Meiburg, B. Kneller, and A. Marsden (2011), Towards inverse modeling of turbidity currents: The inverse lock-exchange problem, *Comput. Geosci.*, *37*(4), 521–529.
- Mahdina, M., B. Firoozabadi, M. Farshchi, A. G. Varnamkhasti, and H. Afshin (2012), Large eddy simulation of lock-exchange flow in a curved channel, *J. Hydraul. Eng.*, *138*, 57–70.
- Meiburg, E., and B. Kneller (2010), Turbidity currents and their deposits, *Ann. Rev. Fluid Mech.*, *42*, 135–156.
- Mulder, T., B. Savoye, and J. P. M. Syvitski (1997), Numerical modelling of a mid-sized gravity flow: The 1979 Nice turbidity current (dynamics, processes, sediment budget and seafloor impact), *Sedimentology*, *44*(2), 305–326.
- Nakajima, T., J. Peakall, W. D. McCaffrey, D. A. Paton, and P. J. P. Thompson (2009), Outer-bank bars: A new intra-channel architectural element within sinuous submarine slope channels, *J. Sediment. Res.*, *79*(12), 872–886.
- Nelson, J. M., and J. D. Smith (1989), Flow in meandering channels with natural topography, in *River Meandering*, AGU Water Resour. Monogr., vol. 12, edited by S. Ikeda and G. Parker, pp. 69–102.
- Nidzicko, N. J., J. L. Hench, and S. G. Monismith (2009), Lateral circulation in well-mixed and stratified estuarine flows with curvature, *J. Phys. Oceanogr.*, *39*(4), 831–851.
- Parker, G., and E. D. Andrews (1985), Sorting of bed load sediment by flow in meander bends, *Water Resour. Res.*, *21*(9), 1361–1373.
- Parker, G., P. Diplas, and J. Akiyama (1983), Meander bends of high amplitude, *J. Hydraul. Eng.*, *109*(10), 1323–1337.
- Parker, G., Y. Fukushima, and H. M. Pantin (1986), Self-accelerating turbidity currents, *J. Fluid Mech.*, *171*, 145–181.
- Parker, G., M. Garcia, Y. Fukushima, and W. Yu (1987), Experiments on turbidity currents over an erodible bed, *J. Hydraul. Res.*, *25*(1), 123–147.
- Parsons, D. R., J. Peakall, A. E. Aksu, R. E. Flood, R. N. Hiscott, S. Besiktepe, and D. Moulard (2010), Gravity-driven flow in a submarine channel bend: Direct field evidence of helical flow reversal, *Geology*, *38*(12), 1063–1066.
- Paull, C. K., W. Ussler, H. G. Greene, R. Keaten, P. Mitts, and J. Barry (2002), Caught in the act: The 20 December 2001 gravity flow event in Monterey Canyon, *Geo Mar. Lett.*, *22*(4), 227–232.
- Peakall, J., W. D. McCaffrey, and B. Kneller (2000), A process model for the evolution, morphology, and architecture of sinuous submarine channels, *J. Sediment. Res.*, *70*(3), 434–448.

- Peakall, J., K. J. Amos, G. Keevil, P. W. Bradbury, and S. Gupta (2007), Flow processes and sedimentation in submarine channel bends, *Mar. Pet. Geol.*, *24*(6), 470–486.
- Peakall, J., I. A. Kane, D. G. Masson, G. Keevil, W. McCaffrey, and R. Corney (2012), Global (latitudinal) variation in submarine channel sinuosity, *Geology*, *40*(1), 11–14.
- Peakall, J., I. A. Kane, D. G. Masson, G. Keevil, W. McCaffrey, and R. Corney (2013), Global (latitudinal) variation in submarine channel sinuosity: REPLY, *Geology*, *41*(5), e288, doi:10.1130/G34319Y.1.
- Piper, D. J. W., and W. R. Normark (1983), Turbidite depositional patterns and flow characteristics, Navy submarine fan, California Borderland, *Sedimentology*, *30*(5), 681–694.
- Pirmez, C., and J. Imran (2003), Reconstruction of turbidity currents in Amazon Channel, *Mar. Pet. Geol.*, *20*(6), 823–849.
- Pyles, D. R., M. Tomasso, and D. C. Jennette (2012), Flow processes and sedimentation associated with erosion and filling of sinuous submarine channels, *Geology*, *40*(2), 143–146.
- Ren, P., B. D. Bornhold, and D. B. Prior (1996), Seafloor morphology and sedimentary processes, Knight Inlet, British Columbia, *Sediment. Geol.*, *103*(3), 201–228.
- Rozovskii, I. (1957), *Flow of Water in Bends in Open Channels*, Acad. of Sci. of the Ukrainian SSR, Israel Prog. Sci. Translations, Jerusalem.
- Savoie, B., N. Babonneau, B. Dennielou, and M. Bez (2009), Geological overview of the Angola–Congo margin, the Congo deep-sea fan and its submarine valleys, *Deep Sea Res., Part II*, *56*, 2169–2182.
- Sequeiros, O. E., et al. (2010), Characteristics of velocity and excess density profiles of saline underflows and turbidity currents flowing over a mobile bed, *J. Hydraul. Eng.*, *136*, 412–433.
- Soulsby, R. (1997), *Dynamics of Marine Sands, a Manual for Practical Applications*, Thomas Telford, London, U. K.
- Straub, K. M., D. Mohrig, B. McElroy, J. Buttles, and C. Pirmez (2008), Interactions between turbidity currents and topography in aggrading sinuous submarine channels: A laboratory study, *Geol. Soc. Am. Bull.*, *120*, 368–385.
- Straub, K. M., D. Mohrig, J. Buttles, B. McElroy, and C. Pirmez (2011), Quantifying the influence of channel sinuosity on the depositional mechanics of channelized turbidity currents: A laboratory study, *Mar. Pet. Geol.*, *28*, 744–760.
- Umlauf, L., and L. Arneborg (2009), Dynamics of rotating shallow gravity currents passing through a channel. Part I: Observation of transverse structure, *J. Phys. Oceanogr.*, *39*(10), 2385–2401.
- Vangriesheim, A., A. Khripounoff, and P. Crassous (2009), Turbidity events observed in situ along the Congo submarine channel, *Deep Sea Res., Part II*, *56*(23), 2208–2222.
- Wells, M. G. (2009), How Coriolis forces can limit the spatial extent of sediment deposition of a large-scale turbidity current, *Sediment. Geol.*, *218*, 1–5.
- Wynn, R. B., B. T. Cronin, and J. Peakall (2007), Sinuous deep-water channels: Genesis, geometry and architecture, *Mar. Pet. Geol.*, *24*(6–9), 341–387.
- Xu, J. P. (2010), Normalized velocity profiles of field-measured turbidity currents, *Geology*, *38*(6), 563–566.
- Xu, J. P., M. A. Noble, and L. K. Rosenfeld (2004), In-situ measurements of velocity structure within turbidity currents, *Geophys. Res. Lett.*, *31*, L09311, doi:10.1029/2004GL019718.
- Xu, J. P., J. P. Barry, C. K. Paull (2013), Small-scale turbidity currents in a big submarine canyon, *Geology*, *41*(2), 143–146.
- Yu, B., A. Cantelli, J. Marr, C. Pirmez, C. O’Byrne, and G. Parker (2006), Experiments on self-channelized subaqueous fans emplaced by turbidity currents and dilute mudflows, *J. Sediment. Res.*, *76*(6), 889–902.